

1 **Coupled Atmosphere–Ocean Reconstruction of the Last**
2 **Millennium Using Online Data Assimilation**

3 **W. A. Perkins¹, G. J. Hakim²**

4 ¹Vulcan, Inc, Seattle, WA USA

5 ²University of Washington, Seattle, WA USA

6 **Key Points:**

- 7 • A new online paleoclimate data assimilation method for atmosphere–ocean recon-
8 struction over the last millennium provides dynamical proxy memory
9 • Reconstructed ocean field validation against instrumental products is largely skill-
10 ful despite a sparse proxy network
11 • Online data assimilation improves the dynamics and low-frequency variability of
12 reconstructed coupled fields relative to offline assimilation

Corresponding author: Walter A. Perkins, wperkins@uw.edu

Abstract

We use online data assimilation to combine information from a linear inverse model of coupled atmosphere-ocean dynamics with proxy records to create a new annual-resolution reconstruction of atmosphere and ocean fields over the last millennium. Instrumental validation of reconstructed sea-surface temperature and 0–700 m ocean heat content shows broad regions of positive spatial correlations, and high correlations (~ 0.6 – 0.9) for global averages and indices of large-scale modes of atmospheric variability. Compared to previous reconstructions, the online reconstructions show global and hemispheric averages with little-to-no millennial-scale trend and global-mean temperatures ~ 0.25 – 0.5 K cooler during early periods (1000–1400 C.E.). The spatial anomaly differences of average temperature between an early (1000–1250 C.E.) and later (1400–1700 C.E.) period show warm anomalies over high-latitude Europe and cool tropical conditions in partial agreement with previous assessments. The addition of online data assimilation, which provides dynamical memory to climate proxy information, is shown to be crucial for adequately characterizing decadal-to-centennial-scale variability of 0–700 m ocean heat content. Furthermore, the climate forecasts provide model-based physical constraints for atmosphere–ocean interaction, which become increasingly important during early periods when less proxy information is available for assimilation.

1 Introduction

Defining the range and mechanisms of low-frequency variability of the Earth system is a crucial factor in understanding climate sensitivity and impacts of future climate change. At least for decadal-to-centennial timescales, the oceans play a central role, acting as an energy reservoir that integrates over the noisier and chaotic atmosphere (e.g., Hasselmann, 1976). While the instrumental record provides a direct account of climate system variability, the length of record is relatively short for investigating slow climate features, especially when considering coupled atmosphere–ocean variability. High-resolution reanalysis products partly extend the record by using numerical models to assimilate observations into atmosphere and ocean fields (e.g., Compo et al., 2011; Balmaseda et al., 2013; Chang et al., 2013; Poli et al., 2016). However, coupled atmosphere–ocean reanalysis products are in the early stage of development (Laloyaux et al., 2018), and reanalysis products are still limited in time due to the lack of observations earlier in the 20th Century. The proxy record, including measurements from trees, ice, corals, sediments, and more, provides an extended account of observed information to investigate decadal and longer climate variability. In order to extend the information contained in proxies from the locations and times to which they pertain, additional information is needed to create a climate field reconstruction (CFR). Early CFR approaches derived the additional information from static statistical relationships derived from the instrumental era (Mann et al., 2009). More recently, paleoclimate data assimilation (PDA) uses dynamical constraints encoded in global climate models (GCMs) to provide the additional information (Hakim et al., 2016; Franke et al., 2017; Okazaki & Yoshimura, 2017; Steiger et al., 2018; Tardif et al., 2019). The CFRs include robust uncertainty quantification and a set of physically consistent spatial fields useful for dynamical inquiry beyond what is feasible from proxies or climate models alone (e.g., Singh et al., 2017). Here we present a new PDA method that uses an approximate GCM to propagate the information extracted from proxies through time, providing dynamical memory, which dramatically improves the reconstruction of low-frequency climate variability. We use these new results to explore low-frequency aspects of coupled atmosphere-ocean dynamics that are not possible with traditional CFRs.

Ensemble-based data assimilation techniques, such as those adapted for PDA, traditionally include a model forecast that translates the updated analysis state to the next time for use as a prior state estimate. This technique, known as “online” assimilation, assumes the forecast model possesses at least some predictive skill at the same timescale

as the time interval between assimilated observations (e.g., Pendergrass et al., 2012). In the PDA context, the lack of significant climate forecast skill and computational expense of performing GCM forecasts has led to most studies omitting the use of a forecast model (Huntley & Hakim, 2010; Bhend et al., 2012; Steiger et al., 2014; Hakim et al., 2016; Franke et al., 2017; Steiger et al., 2018; Tardif et al., 2019). The no-forecast approach, known as an “offline” method (Oke, 2002; Evensen, 2003; Oke et al., 2005, 2007), uses climatological information (e.g., from existing climate simulations) to generate a prior estimate of fields for each analysis time. This technique benefits from being computationally efficient, but the state trajectory over time is solely dependent on available proxy information and is not constrained by physics. The oceans are a potential source of predictability for up to decadal timescales (e.g., Hawkins & Sutton, 2009; Branstator et al., 2012; Zanna, 2012) due to memory and predictable dynamics (e.g., the El Niño Southern Oscillation; ENSO). Thus, the incorporation of a forecast model encapsulating these processes could help constrain low-frequency variability that may not be well represented by proxies (Broecker, 2001; Esper et al., 2002). In addition to providing dynamical memory for information extracted from proxy records, the online PDA approach also produces state-dependent statistics, which spread new proxy information in space and to fields other than those directly related to the proxy. This approach allows the dominant modes of climate variability to evolve in time, in contrast to CFR techniques that are derived from one time period (e.g., the instrumental era, or a GCM simulation of the last millennium).

In this work, we present a substantial improvement to previous PDA methods for CFR with the addition of a simple coupled-climate forecast model to propagate assimilated information in time. Including a model provides a more dynamically consistent coupled reanalysis of atmosphere–ocean fields spanning the last millennium, showcasing the breadth of new field information obtainable from climate proxies, and highlighting features of interest in the long-term temperature and upper-ocean heat content behavior. Section 2 describes the background for data assimilation (DA) and its application for CFRs. Section 3 describes the configuration of reconstruction experiments, including the forward model for the proxy measurements, chosen proxy data, and climate simulation data sources. The results of coupled reconstructions are presented in Section 4 with comparisons to previous reconstructions and validation of ocean fields against Instrumental Era products. We present an illustrative investigation of the climate periods known as the Medieval Climate Anomaly (MCA) and Little Ice Age (LIA), and atmosphere–ocean states related to warm periods over Europe in Section 5. Finally, Section 6 compares the temporal characteristics of online reconstructions with offline and simulation output from GCMs.

2 Data Assimilation Background

In this study, we implement an online version of the Last Millennium Reanalysis framework (LMR; Hakim et al., 2016; Tardif et al., 2019), an open-source codebase for CFR. The framework implements variants of the ensemble Kalman filter (EnKF) to optimally blend information from the proxy record with climate model data. The Kalman update equation, defined as

$$\mathbf{x}_a = \mathbf{x}_b + \mathbf{K}[\mathbf{y} - \mathcal{H}(\mathbf{x}_b)], \quad (1)$$

describes an updated state (e.g., the climate fields of interest), \mathbf{x}_a , as a combination of the prior state estimate, \mathbf{x}_b , with new information from the innovation, $[\mathbf{y} - \mathcal{H}(\mathbf{x}_b)]$, and the Kalman gain, \mathbf{K} . The innovation is the difference between observations (\mathbf{y} ; e.g., proxy measurements) and estimated observations ($\mathcal{H}(\mathbf{x}_b)$) where \mathcal{H} is a function mapping from state space of the prior into the proxy space. Hereafter, the estimated observations are denoted as \mathbf{y}_e for simplicity. The Kalman gain,

$$\mathbf{K} = \mathbf{B}\mathbf{H}^T[\mathbf{H}\mathbf{B}\mathbf{H}^T + \mathbf{R}]^{-1}, \quad (2)$$

113 weights the new contributions from the innovation considering uncertainty in the prior
 114 and observations. Here, \mathbf{B} represents the prior covariance matrix, \mathbf{H} is the linearization
 115 of \mathcal{H} about the prior ensemble mean, and \mathbf{R} is the proxy error covariance matrix. The
 116 Kalman gain term is the key component that translates information from point obser-
 117 vations into full fields through estimated covariance structures. In the LMR framework,
 118 the general DA algorithm used is as follows:

- 120 1. Generate a prior estimate, \mathbf{x}_b , for the current time period. In this case, the prior
 121 state is an ensemble of climate fields joined along a spatial dimension.
- 122 2. Calculate \mathbf{y}_e values using the associated field(s) from the state, \mathbf{x}_b , and a proxy
 123 system model (PSM). For example, a PSM may use a temperature and/or mois-
 124 ture measure from a grid cell to convert to an estimated tree-ring width.
- 125 3. Assimilate available proxy information, \mathbf{y} , for the current analysis time using the
 Kalman update equation (Eq. 1).

126 2.1 Online Paleoclimate Data Assimilation

127 In order to assimilate observations over time, we require a method to generate rel-
 128 evant prior state estimates as a “first guess” of the climate state. In the offline case of
 129 PDA, the prior estimate is often taken as a random draw of states (centered about the
 130 climatological mean) from a long-running climate simulation. The same draw is then used
 131 as a prior for each assimilation period, which results in the reconstructed variability over
 132 time being entirely determined by the assimilated proxy observations. Online assimi-
 133 lation offers a method to propagate information over time by using short-term forecasts
 134 to generate prior estimates for subsequent times. In doing so, some of the memory of pre-
 135 vious proxy information is retained through time. However, online forecasting for PDA
 136 requires large ensembles of millennium-scale climate simulations, posing an exceptional
 137 computational hurdle for most climate model implementations.

138 To make online PDA for ensemble-based techniques feasible, previous work explored
 139 ways to reduce the computational expense while still retaining a skillful model. Recon-
 140 struction studies using a particle filter method of ensemble PDA reduce the computa-
 141 tional expense by incorporating forecasts from Earth system models of intermediate com-
 142 plexity (e.g., Crespin et al., 2009; Goosse et al., 2010; Goosse, 2017; Dubinkina et al.,
 143 2011), or by using a coarsened resolution GCM forecasting at decadal timescales (Matsikaris
 144 et al., 2016b). However, research suggests that online data assimilation using a parti-
 145 cle filter does not necessarily provide a benefit over the offline method for decadal sur-
 146 face temperature reconstructions (Matsikaris et al., 2015, 2016a). Perkins and Hakim
 147 (2017) investigate annual-timescale CFR skill using an ensemble-Kalman-filter-based PDA
 148 method with forecasts of the surface temperature from an empirically fit linear inverse
 149 model (LIM; Penland & Sardeshmukh, 1995). They find the inclusion of a LIM calibrated
 150 on climate model output improves reconstructions of Instrumental Era surface temper-
 151 atures compared to the offline method, and that it retains computational expediency of
 152 the offline method.

153 A LIM provides an empirically derived encoding of system dynamics into two com-
 154 ponents: slow-timescale deterministic linear dynamics, and stochastic noise represent-
 155 ing nonlinearity and unresolved fast-timescales (Eq. B1). The timescale separation of
 156 deterministic and stochastic components is analogous to large-scale climate dynamics
 157 forced by weather. As such, LIMs have been widely used to explore mechanisms of atmosphere-
 158 ocean interactions such as ENSO and the Pacific Decadal Oscillation (PDO; e.g., Alexan-
 159 der et al., 2008; Newman et al., 2011), and as a forecast skill benchmark for decadal sur-
 160 face temperature (Newman, 2013). For the purposes of PDA, a LIM provides a low-cost

161 mechanism to create a stable model approximating the behavior of sophisticated GCMs
 162 and to generate ensembles without requiring any complex state initialization strategy.
 163 In a follow on to Perkins and Hakim (2017), Perkins and Hakim (2020, hereafter denoted
 164 as PH20) describe the use of a LIM as a GCM analog, providing a general method of cal-
 165 ibrating a LIM from a coupled global climate model for ensemble forecasts of multivari-
 166 ate atmosphere–ocean states. They find the multivariate LIM to be skillful out to multi-
 167 year lead times and that it reproduces free-running statistics of large-scale climate dy-
 168 namics indices related to ENSO and the PDO. We use the LIM developed in PH20 as
 169 the forecast model for the online PDA reconstructions we present in this study. For a
 170 technical description of a LIM, forecasting, and our calibration strategy please see Ap-
 171 pendix B.

172 3 Reconstruction Configuration and Data

173 In this study, we perform reconstructions covering a period over the last millen-
 174 nium from 1000–2000 C.E. The climate dynamics used to reconstruct the state for each
 175 experiment depends on the climate model data used to calibrate the LIM. We select two
 176 sources of dynamical information for LIM calibration from the Coupled Model Intercom-
 177 parison Project phase 5 (CMIP5; Taylor et al., 2012) “Last Millennium Experiments”:
 178 the Community Climate System Model version 4 (CCSM4; Landrum et al., 2013) and
 179 the Max Planck Institute Earth System Model (MPI; Giorgetta et al., 2013). The Last
 180 Millennium Simulations cover 850–1850 C.E. and include estimated forcing from green-
 181 house gases, aerosols (primarily volcanic), solar variability, and land-use changes. The
 182 use of two models to reconstruct climate states allows us to assess the robustness of re-
 183 construction results. Our coupled reconstructions include the following fields: 2 m sur-
 184 face air temperature (TAS), precipitation (PR), sea-level pressure (SLP), 500 hPa geopo-
 185 tential height (ZG500), outgoing top-of-atmosphere (TOA) longwave (RLUT), outgo-
 186 ing TOA shortwave (RSUT), sea-surface temperature (SST), sea-surface salinity (SSS),
 187 dynamic ocean surface height (ZOS), and 0–700 m ocean heat content (OHC700m).

188 All fields are regridded to a regular $2^\circ \times 2^\circ$ latitude-longitude grid using bilinear
 189 interpolation and are averaged annually from April to March, except for TAS, which has
 190 additional seasonal averages. Unlike previous offline reconstruction studies (e.g., Hakim
 191 et al., 2016; Tardif et al., 2019), we need to include sub-annual TAS information in the
 192 state to calculate the estimated observations (\mathbf{y}_e) after each climate forecast. We chose
 193 to add all seasonal-average data to the state as individual fields rather than using indi-
 194 vidual calendar months and forming seasonal averages at runtime. The explicit incor-
 195 poration of seasonal-average data carries the benefit of decreasing noise in the covari-
 196 ance estimates, which impacts assimilation and forecast skill (e.g., Tardif et al., 2014).
 197 All fields are detrended to remove long-term climate model drift and converted to anoma-
 198 lies for LIM calibration and reconstruction procedures.

199 After preprocessing the data, we use all fields to calibrate the LIM (Eqs. B2, B3).
 200 We formulate the LIM and perform forecasts in a reduced parameter space using a two-
 201 step empirical orthogonal function (EOF) reduction that PH20 show efficiently preserves
 202 shared aspects of large-scale field variability (Appendix B2). Based on LIM skill test-
 203 ing, we retain 40 degrees of freedom for the CCSM4-LIM (20 multivariate and 20 OHC
 204 EOFs) and 47 for the MPI-LIM (27 multivariate and 20 OHC EOFs). During the re-
 205 construction process, analysis fields (\mathbf{x}_a) are projected into this EOF space, forecast for
 206 1-year using Eqs. B4 and B5, and then back projected into physical space to be used as
 207 the next prior state (\mathbf{x}_b).

208 In the LMR framework (e.g., Tardif et al., 2019), the update equation (Eq. 1) in-
 209 volves the use of an ensemble square-root filter approach (Whitaker & Hamill, 2002), which
 210 serially updates the state one proxy at time. The serial update implementation is rel-
 211 atively straightforward and allows for covariance localization, which is useful to reduce

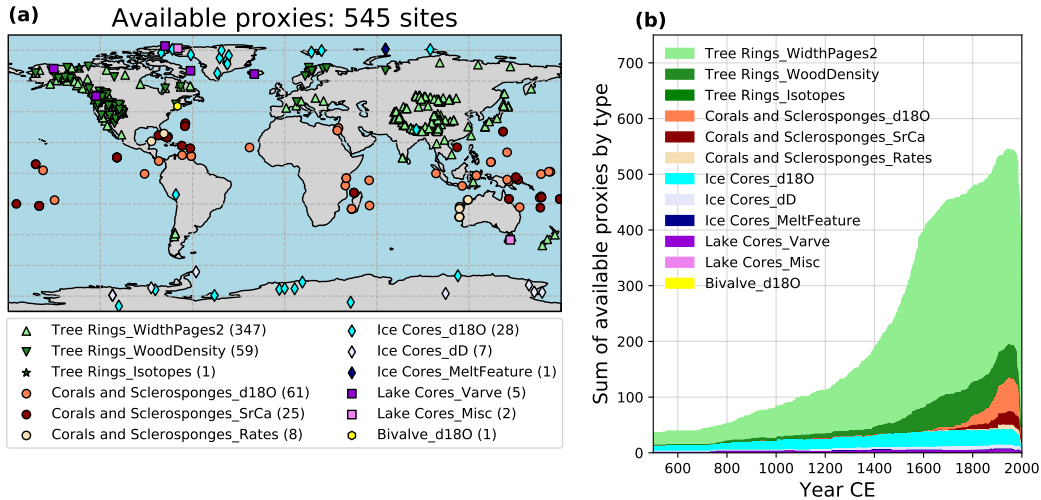


Figure 1. Proxy record spatial distribution (a) and total number of available records separated by type (b) from the PAGES 2k Consortium (2017) database. Proxies shown are those with valid PSMs, which require at least 25-years of overlapping observations with GISTEMP v4 data for calibration.

212 the effects of sampling error at large distances from observations. In the online case, carrying
 213 the fields required for seasonal PSMs increases the state size and computational
 214 expense considerably. To speed up the reconstructions, we solve the update equation using
 215 a new vector solver variant described in Appendix A. This technique reduces the update
 216 problem to the smallest possible space spanned by the ensemble size and number
 217 of proxies, at the expense of no covariance localization on the full-space state (a commonly
 218 used measure to control spurious long-range correlations).

219 The last important factor concerning experiment configuration is the selection of
 220 proxies and proxy system models (PSMs; represented as \mathcal{H}) used to predict the proxy
 221 values from the climate state variables. We use proxy records with annual time resolution
 222 from the PAGES 2k Consortium (2017, PAGES2017) database with a recently updated
 223 Palmyra coral record (Emile-Geay et al., 2013b; Anderson et al., 2019). The PAGES2017
 224 database is a quality-controlled compilation of metadata and proxy records screened for
 225 temperature sensitivity. For each proxy PSM, we fit a linear univariate model using objectively
 226 determined seasonal averages (as in Tardif et al. (2019)) for tree-based proxies and expert-derived
 227 seasonality (PAGES 2k Consortium, 2017) for all other proxy types. (See Appendix C for a
 228 description of the objective testing procedure.) The PSMs are fit against co-located
 229 instrumental temperature data from the NASA Goddard Institute for Space Studies Surface
 230 Temperature Analysis GISTEMP v4 (Hansen et al., 2010) dataset (similarly regridded to a
 231 $2^\circ \times 2^\circ$ grid). Only proxies with an overlap of at least 25-years with instrumental data
 232 are calibrated, which results in 545 usable proxies (Fig. 1).

233 With the calibrated LIM and PSMs, we perform Monte-Carlo (MC) iteration reconstruction
 234 experiments where in each case a 100-member ensemble and 75% of the available proxy
 235 data are assimilated over all times. We run 50 realizations using this resampling strategy
 236 to assess uncertainty related to proxies, such as changing coverage and potential dating
 237 errors, and LIM climate forecasts. Previous work finds that iterative reconstructions in
 238 this manner provide beneficial results (Tardif et al., 2019). The use of 100 ensemble
 239 members is consistent with previous work that shows ensembles of this size reasonably
 240 sample field covariances used in the Kalman gain (Hakim et al., 2016; Tardif

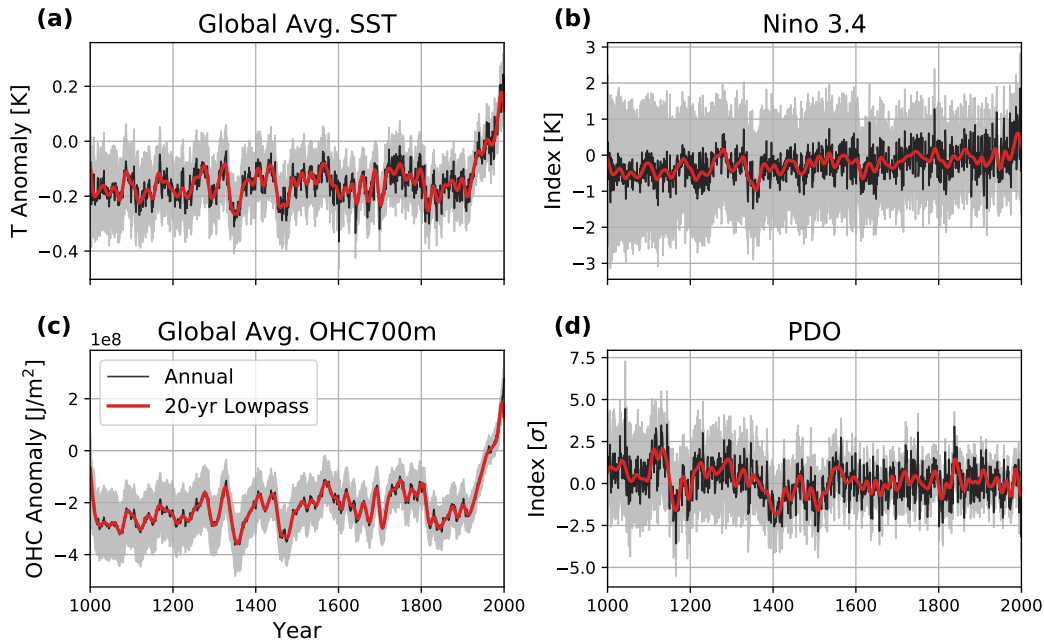


Figure 2. A selection of scalar index ensembles calculated from the annual-average field reconstructions using the CCSM4-LIM including: global average (a) sea-surface temperatures (SST) and (c) 0–700 m ocean heat content (OHC700m), and dynamic indices of the (b) Niño 3.4 region average SST and (d) Pacific Decadal Oscillation (PDO) index. Curves represent the annual ensemble-mean indices taken over all 50×100 members (black) and the associated 95% confidence region (grey shaded), and the smoothed 20-year lowpass filter of the ensemble mean (red).

241 et al., 2019). In addition to online forecasts using LIMs calibrated on the CCSM4 and
 242 MPI Last Millennium Simulations (hereafter referred to as CCSM4-LIM and MPI-LIM),
 243 we perform an offline reconstruction for comparison, which uses climatological draws from
 244 the CCSM4 simulation as a prior. We use a seeding strategy to ensure that the proxy
 245 samples and initial prior ensemble samples are equivalent for a given MC iteration be-
 246 tween the CCSM4-LIM, MPI-LIM and offline experiments.

247 4 Last Millennium Reconstruction using Online Data Assimilation

248 As an overview of reconstructed ocean results, we show area-weighted global average
 249 average temperature and OHC700m, the Niño 3.4 index, and the Pacific Decadal Oscil-
 250 lation (PDO) index (Fig. 2). The Niño 3.4 index is the average SST over the region from
 251 5S–5N and 170W–120W, and the PDO is calculated by projecting the first EOF of North
 252 Pacific (20N–70N and 110E–110W) detrended SST variability from the CCSM4 last mil-
 253 lennium simulation onto the reconstructed SST field. We also provide ensemble-mean
 254 scalars that are smoothed using a 61-sample Lanczos filter (Duchon, 1979) with a cut-
 255 off frequency of 20-years to highlight low-frequency variability in the data. All recon-
 256 structed data are centered with a reference period of 1951–1980 unless stated otherwise.

257 Reconstructed global average SST (Fig. 2a) portray relatively cool conditions for
 258 the majority of the last millennium with apparent decadal-to-centennial-scale (hereafter
 259 referred to as dec-cen) variability (e.g., temperature swings from 1300–1500 and repeated
 260 volcanic cooling events post 1600 C.E). The average SST warms considerably during the

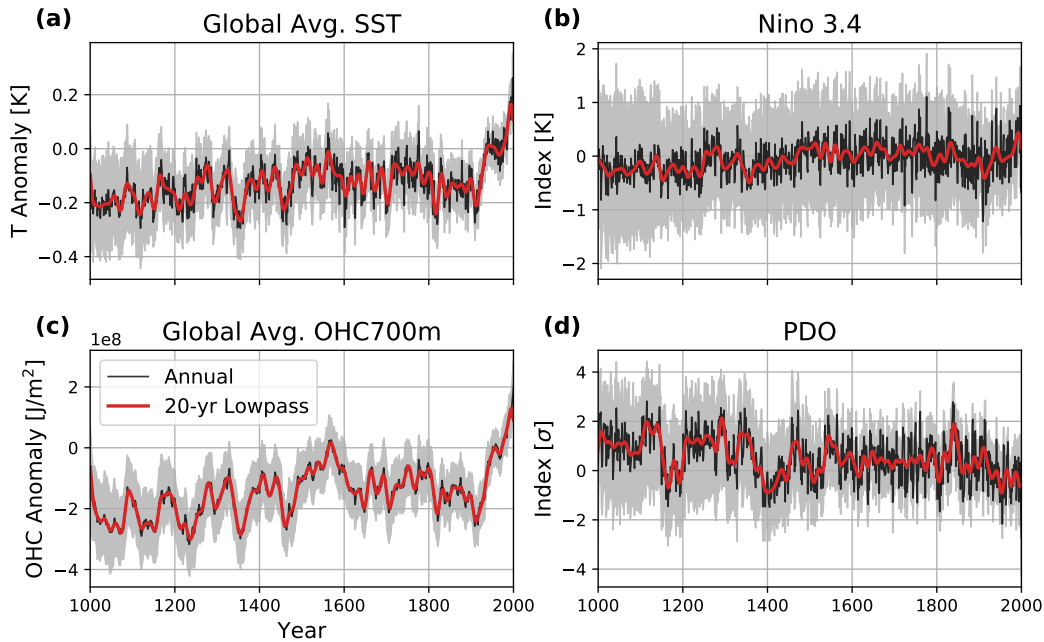


Figure 3. As in Fig. 2 but for the MPI-LIM reconstruction.

261 Instrumental Era ending ~ 0.4 K warmer than the 1000–1850 CE average of approximately
 262 -0.2 K. Additionally, the ensemble-mean SST appears to exit the pre-industrial recon-
 263 structed range of millennial temperatures by the first half of the 20th Century. Notably
 264 absent are global-scale warm anomalies in the early period typically associated with the
 265 Medieval Climate Anomaly (MCA) or millennial-scale cooling present in other field recon-
 266 structions (e.g., Mann et al., 2009; Hakim et al., 2016). We investigate the expres-
 267 sion of the MCA in our reconstruction in Section 5. The reconstructed upper-ocean heat
 268 content (Fig. 2c) shows less interannual variability than SST, but similar dec-cen vari-
 269 ability, which corresponds to the much higher thermal inertia of an ocean layer. Con-
 270 cerning OHC700m thermal inertia, the first few decades of OHC700m show evidence that
 271 there is some “spin-up” time associated with online DA for this field, as the state is drawn
 272 toward observations.

273 The dynamic indices of ENSO (Niño 3.4) and the PDO display the reconstructed
 274 character of known predominant modes of natural variability. The Niño 3.4 index (Fig.
 275 2b) shows relatively stable temperatures over the last millennium with the ensemble aver-
 276 age, suggesting a slight warming trend over time (~ 0.5 K / 1000 yrs). Also evident in
 277 the Niño 3.4 reconstruction is an increase in the positive temperature trend during the
 278 modern era, consistent with global warming. The large span of the 95% confidence re-
 279 gion early in the period is because the Niño 3.4 index is a regional-scale index and there
 280 are relatively few local constraints before the 1600s when more coral records become avail-
 281 able. The PDO index (Fig. 2d) also suggests some dependence on available proxy obser-
 282 vations. Before 1600 C.E., there is pronounced dec-cen variability in the ensemble-
 283 average PDO index with fluctuations of about $2-3 \sigma$ during some periods. After the year
 284 1600, a large number of tree-based information and some corals (Fig. 1) become avail-
 285 able, and the PDO index shows reduced low-frequency variability (Fig. S1). Only con-
 286 sidering reconstructed PDO values after 1600 C.E., there is no distinct long-term trend
 287 or changes to variability between the pre-industrial and modern period.

Scalar indices calculated from the MPI-LIM reconstruction (Fig. 3) give qualitatively similar results as the CCSM4-LIM experiment. Lowpass- filtered scalar correlations with the CCSM4-LIM reconstructions are 0.91 for global average SST, 0.85 for OHC, 0.83 for the PDO, and 0.68 for the Niño 3.4 index, respectively. The temperature-related indices (SST, OHC700m, and Niño 3.4) show some warming into the 16th century followed by cooling into the 17th and 18th century. The warming of the MPI-LIM ensemble-averages (SST and OHC700m) into the 1500s reaches similar temperatures as during the early 20th-Century although the warming occurs over a longer period. Additionally, the OHC700m warm-period before 1600 C.E. is outside of the CCSM4-LIM confidence intervals. This may suggest some underestimation of the LIM forecast variance. The PDO shows large fluctuations in the average index value prior to the 1600s, with similar phasing as in the CCSM4-LIM case. Similarity in the long-term PDO index fluctuations suggest the two online reconstructions reproduce the same ocean state given the same proxy data. However, the change in dec-cen variability after 1600 C.E. is likely due to the sparsity of the proxy data before that time. To illustrate the character of spatial variability from the ocean-atmosphere fields, we provide videos of the evolution of selected fields and the geographic distribution of available proxies over time (Movies S1 and S2). In these field sequences, the coupled variability associated with ENSO and with slower modes of variability in the North Atlantic and Pacific are prominent features, as well as the global-scale warming during the 20th Century.

4.1 Instrumental Validation

We now validate the field reconstructions during the instrumental period for SST and OHC700m spatial fields and related scalar quantities. Comparison products include the following: Hadley EN4 v4.2.1 (Good et al., 2013), a quality-controlled and objectively interpolated dataset based on ocean profile measurements from 1940–2000 C.E., the Geophysical Fluid Dynamics Laboratory Ensemble Coupled Data Assimilation (GFDLECDA; Chang et al., 2013), a coupled climate model reanalysis using ocean observations from 1960–2010 C.E., and the European Center for Medium-range Weather Forecasting (ECMWF) ORA-20C dataset covering 1900–2010 (de Boissésou et al., 2018), an ocean-field reanalysis for use as initial conditions in ECMWF coupled reanalysis product (Laloyaux et al., 2018). For El Niño, PDO, and OHC comparison, we also use the Earth System Research Laboratory Niño 3.4 time series (1950–2018, accessed Apr. 19, 2019), the Mantua et al. (1997) PDO index hosted by the Joint Institute for Study of the Atmosphere and Ocean (research.jisao.washington.edu/pdo/PDO.latest.txt, accessed Apr. 19, 2019), a gridded OHC estimate optimally interpolated using information from CMIP5 historical simulations, and an estimate of OHC over the full Instrumental Era using observed SSTs and a passive ocean transport model (Cheng et al., 2017; Zanna et al., 2019).

Temporal gridpoint correlations with instrumental products show large-scale agreement with SST and more regionally dependent agreement for OHC700m (Fig. 4). SST correlations (Fig. 4, column a) are largely positive in the tropics, especially the tropical Pacific Ocean, less correlated in the Southern Ocean regions and Northwest Pacific, and uncorrelated-to-anti-correlated in the Labrador Sea and North Atlantic region south of Greenland and Iceland. SST correlations display better spatial agreement with the two model-reanalysis experiments (GFDLECDA, ORA-20C) than the observation-only data (HadleyEN4). Correlations for OHC700m (Fig. 4, column b) similarly show the tropical Pacific Ocean as a region with more agreement between the reconstruction and instrumental products. Additionally, OHC700m correlations are moderately positive in the subtropical Atlantic Ocean and weak-to-moderately positive in the mid-latitude Southern Ocean areas when comparing with the four instrumental products. The HadleyEN4 dataset shows the lowest correlations, especially in the Southern Hemisphere, with the CCSM4-LIM reconstructed OHC700m. In general, more regions of small or negative correlations are apparent for OHC700m, but the North Atlantic and Labrador Sea region again is a common region of anti-correlation with instrumental products. We note that

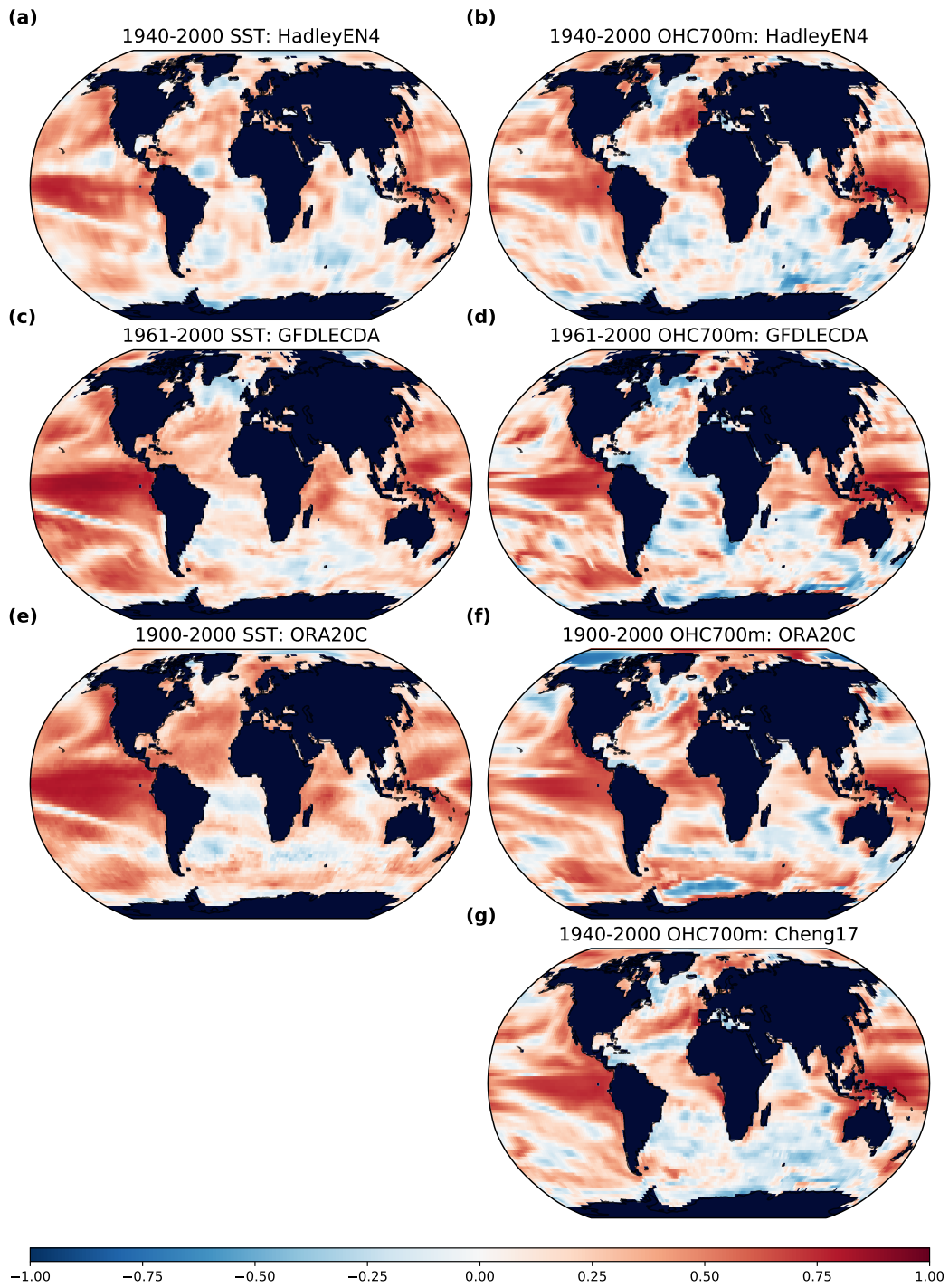


Figure 4. Detrended temporal gridpoint correlations of the LMR Online (CCSM4-LIM) reconstruction with Instrumental Era observational and reanalysis products for SST (column a) and OHC700m (column b). Correlations are calculated against Hadley EN4 data (a, b; 1940–2000), GFDLECD (c, d; 1961–2000), ORA-20C (e, f; 1900–2000), and Cheng2017 (g; OHC only, 1940–2000)

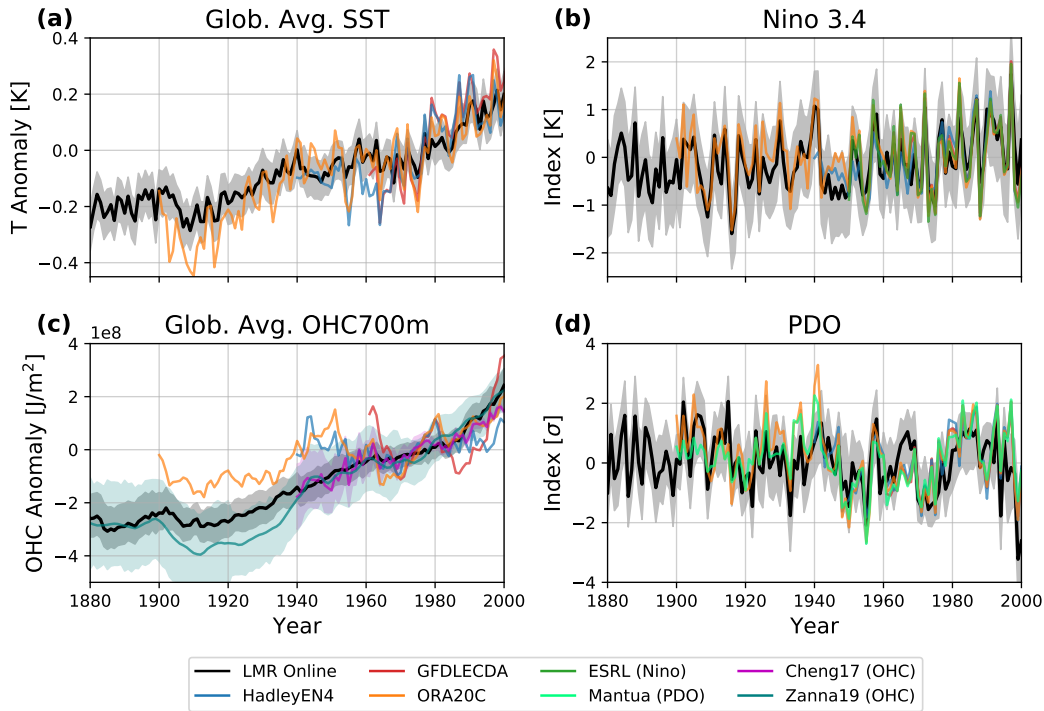


Figure 5. Scalar index comparison between the LMR Online (CCSM4-LIM) reconstruction (black with 95% confidence bounds in grey shading) and instrumental products for (a) SST, (b) Niño 3.4, (c) OHC700m, and (d) PDO. The HadleyEN4, GFDLECD, and ORA-20C products are compared in all cases. Additionally, ESRL Niño 3.4 data, the Mantua et al. (1997) PDO index, and Cheng et al. (2017) and Zanna et al. (2019) OHC data are compared. Error bounds ($\pm 2\sigma$) are shown for the Cheng17 and Zanna19 OHC700m data.

341 OHC observations were generally sparse during the 20th century before the implemen-
 342 tation of the ARGO observing array during the late 1990s (Riser et al., 2016). There-
 343 fore, observationally-based spatial products have large uncertainties for OHC700m dur-
 344 ing the 20th Century and considerable discrepancies (e.g., see Fig. S2 for instrumen-
 345 tal product spatial correlation comparisons). The southern Atlantic and Indian oceans show
 346 up as a region of low correlation for both SST and OHC700 likely due to the large dis-
 347 tance from the assimilated proxy observations. However, this is also the region that dis-
 348 plays the most uncertainty between observational products (e.g., Fig S2). We also val-
 349 idate the MPI-LIM SST and OHC700m against these products and find similar corre-
 350 lation patterns as those described for CCSM4-LIM reconstructions (Fig. S3).

351 Figure 5 shows a comparison of instrumental scalar indices, and Table 1 shows the
 352 associated correlation values. The reconstructed global average SST values (Fig. 5a) fol-
 353 low the decadal trajectory of the instrumental products but also show smaller amplitude
 354 interannual variability. Additionally, the small 95% confidence interval for SSTs relative
 355 to the validation data mismatch suggests the ensemble variance of this scalar measure
 356 is underestimated. SST correlations with the instrumental products are generally high
 357 with values between 0.8–0.9. As in the spatial comparison, the LMR Online reconstruc-
 358 tion agrees best with the two reanalysis products (GFDLECD and ORA-20C). Despite
 359 the lack of interannual anomaly amplitude for global-average SST, the Niño 3.4 index
 360 (Fig. 5b) matches the comparison products well for both phase (correlations between
 361 0.8–0.87) and amplitude. Upper-ocean heat content products (Fig. 5c) have more dis-

Table 1. LMR Online (CCSM4-LIM) reconstruction scalar correlations with instrumental products.

Product	Glob. Avg. SST	Glob. Avg. OHC700m	Nino 3.4	PDO
HadleyEN4	0.80	0.27	0.79	0.61
GFDLECD A	0.89	0.58	0.87	0.56
ORA20C	0.90	0.79	0.80	0.63
ESRL	–	–	0.84	–
Mantua	–	–	–	0.58
Cheng17	–	0.94	–	–
Zanna19	–	0.98	–	–

362 agreement among them, but the LMR Online reconstruction is strikingly similar to the
363 Cheng17 (correlation of 0.94) and Zanna19 (correlation of 0.98) data. These two data
364 products share the distinction of using a passive style of model–observations blending.
365 The other products (HadleyEN4, GFDLECD A, and ORA-20C) tend to have much larger
366 decadal-scale variability and differences of the global average OHC700m trajectory. Fi-
367 nally, the PDO comparison (Fig. 5d) shows that the CCSM4-LIM reconstruction repro-
368 duces the decadal-scale changes of the PDO, but is less skillful for interannual PDO vari-
369 ability (correlations near 0.6 for all products). The 95% confidence interval is generally
370 close to encompassing the interannual instrumental PDO data, which suggests the un-
371 certainties of the reconstructed PDO estimate are reasonable.

372 The MPI-LIM reconstruction scalar validation (Fig. S4) shows similar global av-
373 erage performance based on correlation but less skill for the dynamic indices. The re-
374 constructed global average SST and OHC700m show a noticeable pause in warming from
375 1940–1970 C.E. and do not warm as strongly towards the end of the reconstruction pe-
376 riod. The reconstructed Niño 3.4 in the MPI-LIM case has smaller amplitude interan-
377 nual anomalies, and correlations with instrumental products of 0.72–0.78 (Table S1). The
378 reconstructed PDO, in this case, shows less clear agreement with decadal-scale variabil-
379 ity and the correlations for the shorter-length comparisons (HadleyEN4, GFDLECD A,
380 Mantua) decrease to 0.24–0.42. The differences in reconstruction performance of dynamic
381 indices suggest the MPI-LIM produces less representative reconstructed fields in these
382 regions, which could be related to the character of the MPI-LIM dynamics, or how proxy
383 information is weighted given the forecast ensemble characteristics.

384 4.2 Comparison to previous reconstructions

385 To put our reconstruction in the context of previous research, we show the LMR
386 Online (CCSM4-LIM) reconstruction compared to other proxy-based reconstructions (Fig.
387 6). We apply a 20-year lowpass filter to all data except for SST, which is averaged to
388 100-year intervals to correspond with the SST estimates from McGregor et al. (2015).
389 Note that the comparison SST data (McGregor et al., 2015) are re-averaged to 100-year
390 intervals (as opposed to the 200-year intervals they present) using that study’s associ-
391 ated code and data.

392 The Northern Hemisphere (NH) average temperature reconstructions (Fig. 6a) show
393 closer correspondence from roughly 1500 C.E. onwards with LMR Online on the cooler
394 end of the distribution. Notable cooling events in the NH temperature (e.g., in the 1300s
395 and 1400s) display a more extensive range of hemisphere average temperature variabil-
396 ity and the LMR temperatures are generally 0.25–0.5 K cooler than other reconstruc-
397 tions in the early portion of the last millennium. Cooler NH temperatures suggested by
398 our reconstruction are closer in agreement with borehole estimates (Pollack & Smerdon,

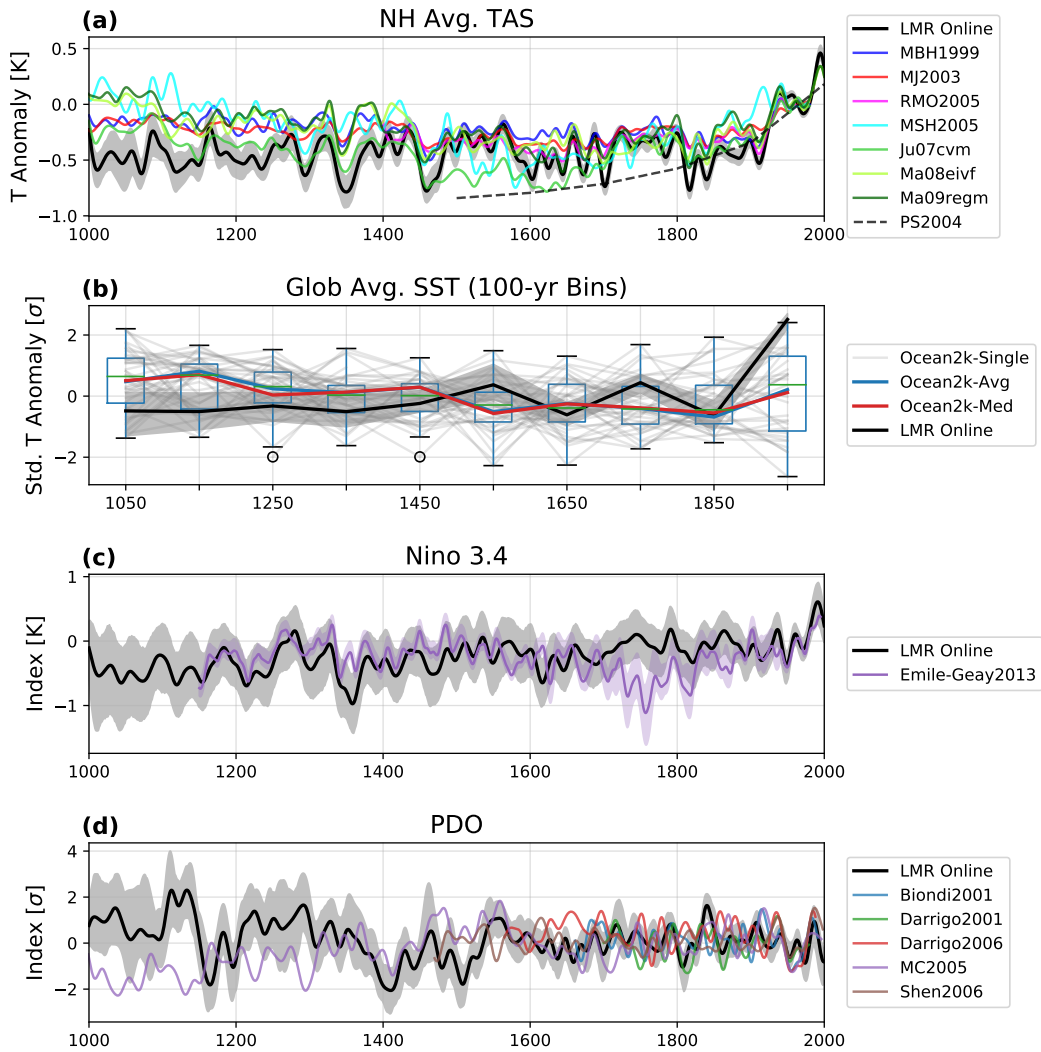


Figure 6. A comparison of LMR Online (CCSM4-LIM) reconstructed scalar indices with previous reconstructions. Northern hemisphere average TAS (a) is compared between LMR Online (black; grey shading for 95% confidence region) and the following studies: MBH1999: Mann et al. (1999), MJ2003: Mann and Jones (2003), PS2004: Pollack and Smerdon (2004), RMO2005: Rutherford et al. (2005), MSH2005: Moberg et al. (2005), Ju077cvm: Juckes et al. (2007), Ma08eivf: Mann et al. (2008), and Ma09regm: Mann et al. (2009). Global average SST (b) is compared with McGregor et al. (2015), a compilation of 57 100-year bin-averaged sediment records with the basin-weighted mean standard anomaly (blue), median standard anomaly (red), and box-whisker plots displaying the inner-quartile range (IQR) with $1.5 \times \text{IQR}$ whiskers at each time interval. The Niño 3.4 index (c) is compared against index reconstructions from Emile-Geay et al. (2013a) where the solid line is the average of three reconstructions they present and shading denotes the range. The PDO (d) is compared with collection of index reconstructions using proxies with a variety of regional coverage (Biondi et al., 2001; D’Arrigo et al., 2001; MacDonald & Case, 2005; D’Arrigo & Wilson, 2006; Shen et al., 2006).

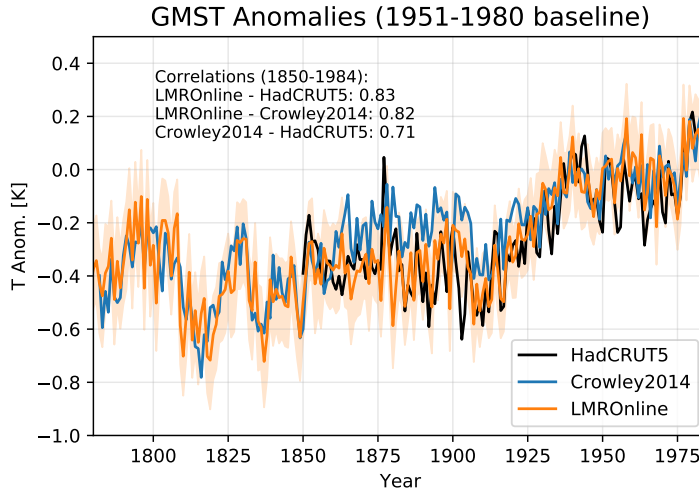


Figure 7. A comparison of LMR Online (CCSM4-LIM) reconstructed global mean surface air temperature (orange with 95% confidence region shaded) against the Crowley et al. (2014) ENSO-tuned global composite reconstruction (blue) and HadCRUT5 (Osborn et al., 2021) observational data (black).

399 2004), and the tree-based estimates from Juckes et al. (2007). Global average SST (Fig.
 400 6b) estimated from sediment cores generally has a wider uncertainty range than the LMR
 401 Online reconstructed SST owing to fewer single-location measurements and large differ-
 402 ences in temporal recording resolution of the different cores. Throughout the 1000-year
 403 reconstruction, our reconstructed SST values fall within the whiskers ($1.5\times$ inner-quartile
 404 range) for all times except during the last 100-year interval where global warming has
 405 considerable influence, and sediment cores lack information. LMR Online global aver-
 406 age SSTs are cooler earlier in the reconstruction period compared to the Ocean2k me-
 407 dian and mean values.

408 The Niño 3.4 index shows limited agreement with Emile-Geay et al. (2013a, referred
 409 to as EG13) while the PDO index shows general disagreement with the five comparison
 410 studies (Biondi et al., 2001; D’Arrigo et al., 2001; D’Arrigo & Wilson, 2006; MacDon-
 411 ald & Case, 2005; Shen et al., 2006) outside of the Instrumental Era. Comparing the Niño
 412 3.4 index (Fig. 6c), the EG13 reconstruction is mostly within the uncertainty bounds
 413 of the LMR Online reconstruction except during the period from approximately 1700–
 414 1900 where the EG13 reconstructed temperatures are about 0.5–1.0 K cooler. The pe-
 415 riod of divergence (1700–1900) occurs over a time where the number of available proxy
 416 records markedly increases in both reconstructions. We note that the EG13 large-scale
 417 tropical multiproxy network does overlap with the records used in our reconstruction ex-
 418 periments, but the number of used proxies in the EG13 network is much smaller (36 to-
 419 tal records). The PDO index comparison (Fig. 6d) shows that the reconstructions mostly
 420 disagree in signal phasing. Correlations between the experiments (Fig. S5) show the D’Arrigo
 421 et al. (2001) reconstruction has the highest agreement with the CCSM4-LIM reconstructed
 422 PDO with a value of ~ 0.4 . Otherwise, most correlations are quite low or even anti-correlated
 423 (e.g., MacDonald & Case, 2005). The Biondi et al. (2001) reconstruction has the broad-
 424 est agreement across records, but even that agreement is relatively low (correlations be-
 425 tween 0.2–0.5).

426 For additional perspective, we include a comparison of annual global-mean surface
 427 temperature from our online DA reconstruction with that of Crowley et al. (2014), which

they describe as a “baseline” reconstruction employing minimal proxy processing. The Crowley et al. (2014) method uses a geographically broad and fixed proxy network over time. Proxy data are centered, standardized, zonally averaged, and then linearly regressed against instrumental temperature data (HadCRUT3) to reconstruct temperature from the proxy composites before the instrumental period. This definition is analogous to the inverse of the \mathcal{H} operator in (Eq. 1), taking climate as a linear function of the proxies (\mathcal{H} relates proxy values linearly to climate). Overall, the two reconstructions are quite similar with a correlation of 0.82 over 1850–1984 C.E., in-phase multi-decadal variability, and a similar magnitude of overall warming into the late 20th century. The two reconstructions slightly diverge around 1860–1910 C.E. where the Crowley reconstruction is about 0.1–0.2 C warmer. When comparing to HadCRUT5 instrumental temperature data (Osborn et al., 2021), the LMR Online reconstruction outperforms the Crowley baseline with a higher correlation (0.83 compared to 0.71 for Crowley) and better agreement with observations through 1860–1910 C.E. where Crowley data shows slightly higher temperatures. We emphasize that the Crowley composite reconstruction is calibrated directly to large-scale zonal averages of HadCRUT3 data, while our reconstruction derives indices from reconstructed full-fields informed by locally assimilated proxy data.

5 Medieval Climate Anomaly in LMR Online

The “Medieval Climate Anomaly” (MCA) is an often targeted period (e.g., 950–1250 C.E.) for investigating the mechanisms and magnitude of natural climate variability before the Industrial Era (see review by Diaz et al., 2011). Documentary evidence (Lamb, 1965) and reconstructions based on proxy records (e.g., Mann et al., 2008, 2009; Ljungqvist, 2010) suggest the possibility of extended regional-to-hemispheric warm periods during the MCA. Mann et al. (2009), using a multi-proxy statistical technique, estimate the spatial character of the temperature transition from the MCA into the “Little Ice Age” (LIA), a period of cool climate conditions roughly between the 1400s and 1800s. They find the MCA–LIA difference is defined by broad warmth with a La Niña-like temperature pattern in the tropical Pacific, and that potential mechanisms for this pattern are related to forcing from ENSO and high-latitude atmospheric circulation variability. Goosse, Cressin, et al. (2012) and Goosse, Guiot, et al. (2012) examine climate dynamics of the MCA period over Europe and the northern hemisphere using the ensemble particle filter PDA method. Spatial reconstructions coupled with information from regional proxy assessments suggest possible mechanisms for the MCA–LIA transition including changes in North Atlantic SST and atmospheric circulation (e.g., Trouet et al., 2009), teleconnections related to cool tropical Pacific temperatures (Cobb et al., 2003; Mann et al., 2009), feedbacks related to solar variability (Ammann et al., 2007; Meehl et al., 2009; Goosse, Cressin, et al., 2012) and volcanic activity (Atwood et al., 2016). However, uncertainties related to the proxy network and reconstruction methodology can produce significant differences in estimated spatial characteristics of the MCA (Wang et al., 2015). Furthermore, recent work utilizing statistical and PDA-based CFR techniques finds little evidence of globally coherent warm or cold extremes before 20th Century warming (Neukom, Steiger, et al., 2019). As an example, we provide a short investigation of the LMR Online reconstruction of the MCA–LIA transition and field relationships with average temperatures over the European region.

The reconstructed NH average temperature, as previously described, shows relatively cool temperatures throughout the pre-industrial period (Figs. 8a, 8b). However, when averaging temperature over the European (EU) region (40–80N, 20W–40E), decadal-scale warming events within the MCA period are apparent. In the CCSM4-LIM reconstruction (Fig. 8a), the EU warm events reach a magnitude about half as large as the early 20th Century warming. The MPI-LIM reconstruction (Fig. 8b) also shows decadal-scale warm periods during the MCA consistent with CCSM4-LIM results.

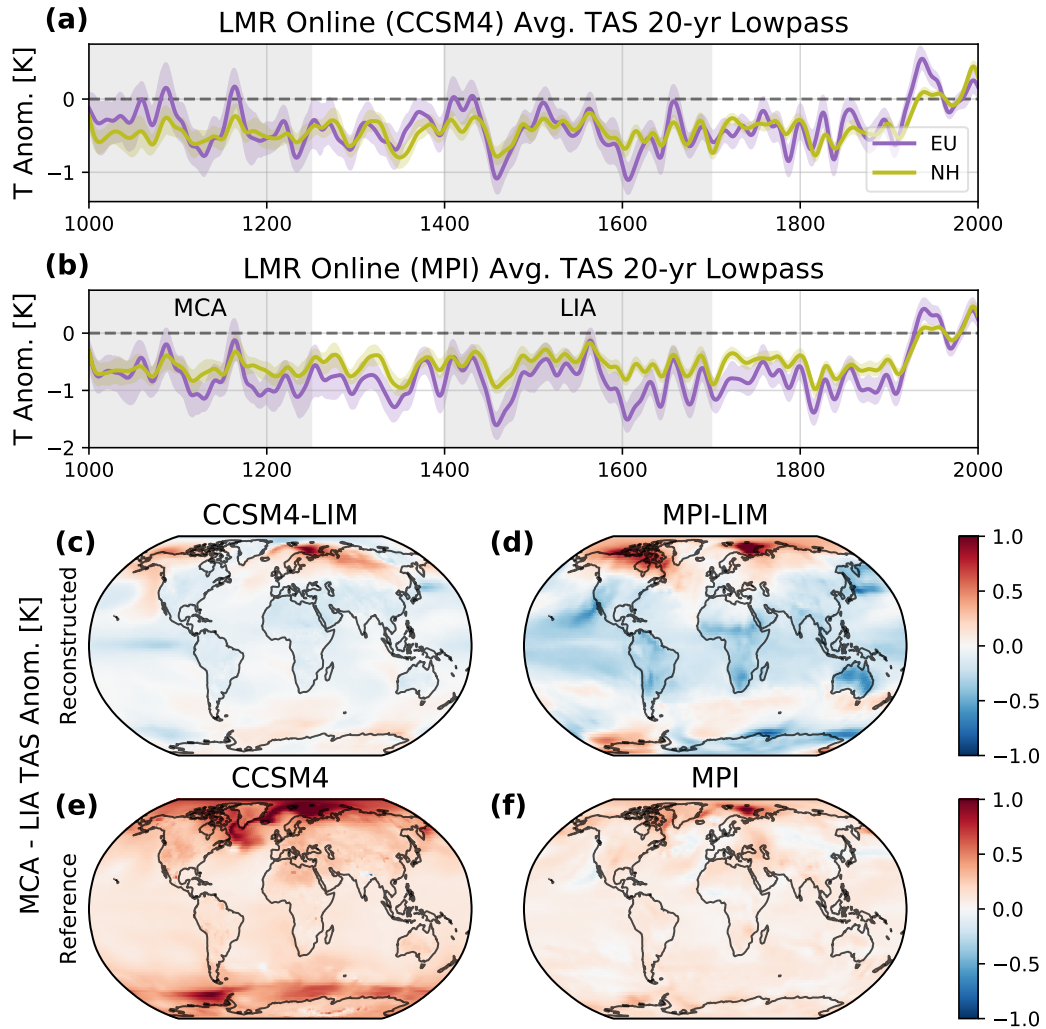


Figure 8. Comparisons between Europe (40–80N, 20W–40E) and North Hemisphere lowpass-filtered average TAS anomalies (centered about 1951–1980 C.E.) for the (a) CCSM4-LIM and (b) MPI-LIM reconstructions. As in Mann et al. (2009), spatial differences between the reconstructed (1000–1250 C.E.) and the LIA (1400–1700 C.E.) time periods are shown for (c) CCSM4-LIM and (d) MPI-LIM reconstructions and for reference (e) CCSM4 and (f) MPI Last Millennium Simulations.

479 Spatial differences in the reconstructed TAS field between the MCA and LIA pe-
 480 riods for the CCSM4-LIM and MPI-LIM reconstruction experiments are shown in Figs
 481 8c and 8d. Both reconstructions have positive temperature anomalies over north-
 482 ern Europe with a maximum occurring over the Barents Sea in the sea-ice transition re-
 483 gion, some expression of higher-latitude warming in North America, and colder tropi-
 484 cal regions. However, there is no evident global-scale warmth, which agrees with results
 485 presented by Neukom, Steiger, et al. (2019) but stands in contrast to the reference GCM
 486 simulations (Fig. 8e and 8f). The patterns of the reference simulations for the MCA-
 487 LIA difference presents as mostly global-scale warming, whereas the reconstructions are
 488 more regionally distinct, with warmer conditions at high-latitudes and colder in the trop-
 489 ics.

490 Considering the two reconstructed MCA-LIA patterns (Figs. 8c, 8d), there are sub-
 491 stantial differences in the spatial character of anomalies outside of Europe. The CCSM4-
 492 LIM reconstruction MCA-LIA difference has warming localized to Alaska and Canada
 493 with a positive PDO expression in the North Pacific and a La Niña-like state in the trop-
 494 ical Pacific. The MPI-LIM/MCA-LIA difference has broad warming across the entire
 495 Arctic region with broadly cold tropical and North Pacific temperatures. Consistent with
 496 the sentiment expressed in Wang et al. (2015), differences in the regional expression of
 497 temperature anomalies reinforce the notion that result robustness to methodological deci-
 498 sions should be considered along with reconstruction results.

499 Both the CCSM4-LIM and MPI-LIM reconstructions point to a warm anomaly in
 500 the vicinity of northern Europe during the MCA. We now investigate how temperatures
 501 in Europe (20-year lowpass filtered) covary with the coupled fields of SST/ZG500 and
 502 OHC700m/SLP using regression analysis during 1000–1850 C.E. (Fig. 9). In the CCSM4-
 503 LIM reconstruction, warm temperatures in the EU region are related to generally warm
 504 SSTs (Fig. 9a) with maximum warmth in the Norwegian and Barents Sea and warmer
 505 SSTs in the Gulf Stream region. Upper-level ZG500 field shows an annular pattern of
 506 increased mid-latitude heights with maxima situated over the North Atlantic, Europe,
 507 North Pacific, and North America. Lower values of ZG500 over the Arctic suggest a strength-
 508 ening of the upper-level circulation, which is reminiscent of a positive-phase Arctic Os-
 509 cillation (AO; Wallace & Thompson, 1998). The positive-phase AO is highly correlated
 510 with a positive North Atlantic Oscillation (NAO) phase (e.g., Ambaum et al., 2001), which
 511 is associated with warmer temperatures and enhanced storminess over the EU region in
 512 modern times (Rogers, 1997; Trigo et al., 2002). The regression on the OHC700m field
 513 (Fig. 9b) shows similarly located regions of warm anomalies associated with EU-region
 514 warmth, and the SLP regression suggests the Arctic circulation anomaly strengthens near
 515 the surface. Significance tests show that the SST and OH700m anomalies are significant
 516 at the 95% thresholds (Figs. S8a, S8b). Significant aspects of the ZG500 field are asso-
 517 ciated with the positive height anomaly maxima, but SLP significance is limited to the
 518 North Atlantic and the central Arctic regions.

519 The MPI-LIM reconstruction regressions (Figs. 9c, 9d) mostly disagree with the
 520 CCSM4-LIM results over the North Pacific, but display some similar results as in the
 521 CCSM4-LIM case in other regions. Positive SST and OHC700m anomalies in the Nor-
 522 wegian and Barents Sea are associated with warm EU average temperature. The OHC700m
 523 field has negative anomalies south of Greenland as opposed to more neutral heat con-
 524 tent in the CCSM4-LIM reconstruction, but these regions are not significantly related
 525 to EU average temperature (Fig. S8c). For ZG500 (Fig. 9c), there are similarly four cen-
 526 ters of height local maxima in the mid-latitudes, but in contrast to the CCSM4-LIM case,
 527 there is an increase in ZG500 over the Arctic. At lower levels, the SLP regression im-
 528 plies lower pressure over the Arctic region with the local maxima located over Green-
 529 land and Arctic regions north of EU and Asia. Lower Arctic SLP and an increase in Arc-
 530 tic ZG500 suggests warmer temperatures in Europe are associated with higher atmospheric
 531 thickness over the Arctic. However, the SLP relationships with EU temperature are not

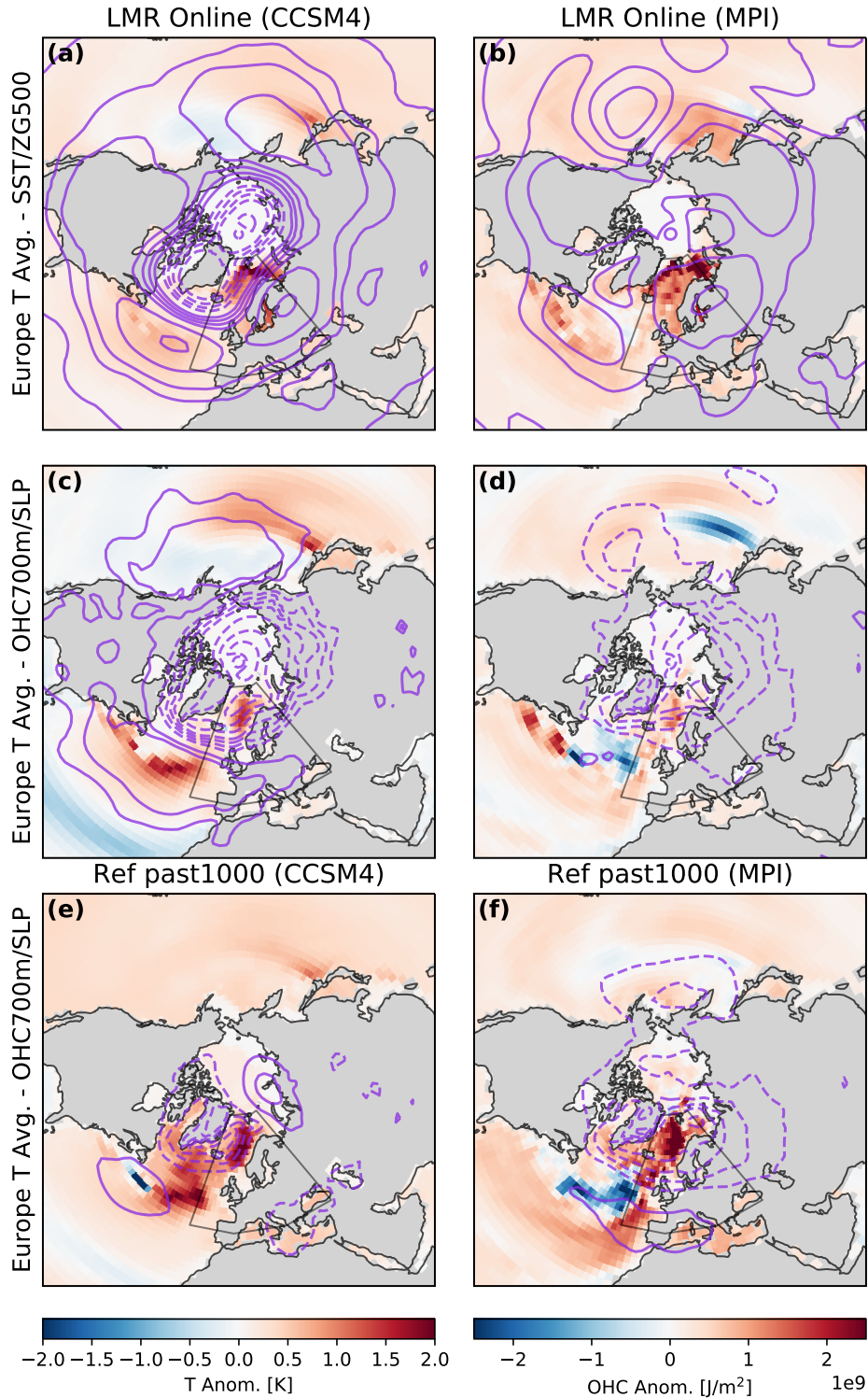


Figure 9. Regression of the Europe average TAS (region denoted by black box) from 1000–1850 C.E. onto fields of (row a) SST/ZG500 and (rows c and e) OHC700m/SLP for the (a, c) CCSM4-LIM and (b, d) MPI-LIM reconstructions, and (e) CCSM4 and (f) MPI reference last millennium simulations. ZG500 field contour levels are incremented by 2.5 m from 2.5–10 m and 5 m from 10–20 m for positive (solid) and negative (dashed) values. SLP field contour levels are incremented by 0.25 hPa from 0.25–1.0 hPa and by 0.5 hPa from 1.0–2.5 hPa. All data are 20-year lowpass filtered prior to calculating the regression.

532 significant at the 95% confidence level (Fig. S8d). The CCSM4-LIM and MPI-LIM re-
 533 construction regressions suggest a strengthened lower-level Arctic circulation anomaly
 534 in the lower atmosphere along with the warmer regional SSTs and OHC700m anom-
 535 lies. Furthermore, the regression relationships are notably different from those derived
 536 from the reference CCSM4 Last Millennium simulations, which tend to be much more
 537 regional in scale (Fig. 9e). The change in character of the reconstructed field relation-
 538 ships with EU temperature suggests that proxy assimilation adds new information to coupled-
 539 field variability over the past 1000 years.

540 6 Temporal Constraints in the Online Technique

541 A motivating factor in pursuing online assimilation for climate reconstruction is
 542 the long-term predictability related to ocean dynamics and memory (Goosse, 2017). With
 543 predictive skill on timescales longer than the temporal resolution of the proxies (e.g., Hawkins
 544 & Sutton, 2009; Perkins & Hakim, 2020), adding a forecast model preserves information
 545 assimilated at previous times. In this section, we provide an assessment of changes to
 546 reconstructed state memory and dynamics for the ocean fields by comparing the online
 547 results with the offline results and the reference GCM simulations. For the offline recon-
 548 struction, proxy data is the only information governing variability and memory over time.
 549 In contrast, the online reconstructions have LIM dynamics, which persist and constrain
 550 climate signals when less proxy data are available. The reference models provide a com-
 551 parison between the variability that the LIM dynamics are calibrated to emulate, and
 552 the influence of the LIM coupled to proxy assimilation. Where applicable, we compare
 553 time periods pre- and post-1600 C.E. in order to assess the dynamics with fewer and more
 554 proxies, respectively, available to constrain the reconstruction.

555 Comparing the online CCSM4-LIM results with the offline CCSM4 reconstruction
 556 of lowpass-filtered global average TAS, SST, and OHC700m (Fig. 10) reveals cooler con-
 557 ditions (~ 1000 – 1600 C.E.), a tightened confidence interval, and larger dec-cen fluctu-
 558 ations in the online results. Because both the online and offline LMR reconstructions use
 559 the same proxy information, TAS and SST signal phasing between the two reconstruc-
 560 tions is high (correlations near 0.9). Additionally, the online reconstruction results for
 561 TAS and SST generally fall within the confidence interval of the offline results. However,
 562 for OHC700m, differences in dec-cen variability are more substantial. Overall, the ad-
 563 dition of temporal memory and dynamical information results in cooler temperatures early
 564 in the reconstruction period, diminishing the millennial-scale cooling trend compared to
 565 the offline case. Even though low-frequency variability may not be well represented by
 566 annually-resolved proxies, we recover an estimate of low-frequency variations via assim-
 567 ilation and the slow-timescale dynamics of the LIM.

568 To test if the cooler reconstructed temperature during the early period of the last
 569 millennium are an artifact of the LIM, we performed two additional experiments. First,
 570 to test whether the inclusion of volcanic events in the LIM calibration may result in sus-
 571 tained artificially cool temperatures during low proxy-information periods, we performed
 572 an equivalent reconstruction experiment using a LIM calibrated on the CCSM4 pre-industrial
 573 control (piControl) simulation without forcing (see Section S2 for details). Results show
 574 that the piControl-LIM experiment still displays a relatively cool early period with no
 575 millennial-scale cooling trend (Fig. S6). Second, we tested sensitivity to the initializa-
 576 tion time by starting another CCSM4-LIM reconstruction from the year 1 C.E. This ex-
 577 periment produced nearly identical reconstruction results from 1000 C.E. onward (Fig.
 578 S7). Finally, we note that, by construction, the LIM mean state is zero, and all anom-
 579 alies decay with time. For example, when initializing a deterministic (no-noise) LIM fore-
 580 cast from the CCSM4-LIM reconstructed states, all global average TAS anomalies decay
 581 to nearly zero on the order of a decade (not shown). Taken together, these results
 582 strongly suggest that the relatively cool reconstructed states are a result of system mem-
 583 ory that is consistently reinforced by information from proxies.

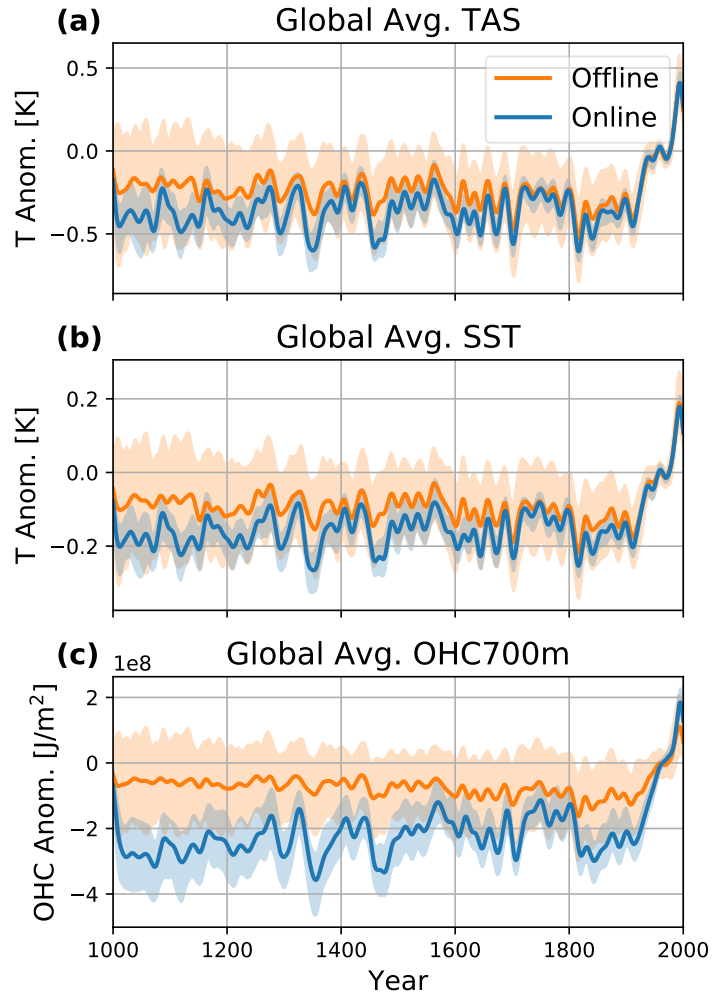


Figure 10. A comparison of the offline and online CCSM4-LIM reconstructions for lowpass filtered global average 2 m surface air temperature (TAS), sea-surface temperature (SST), and 0-700m ocean heat content (OHC700m).

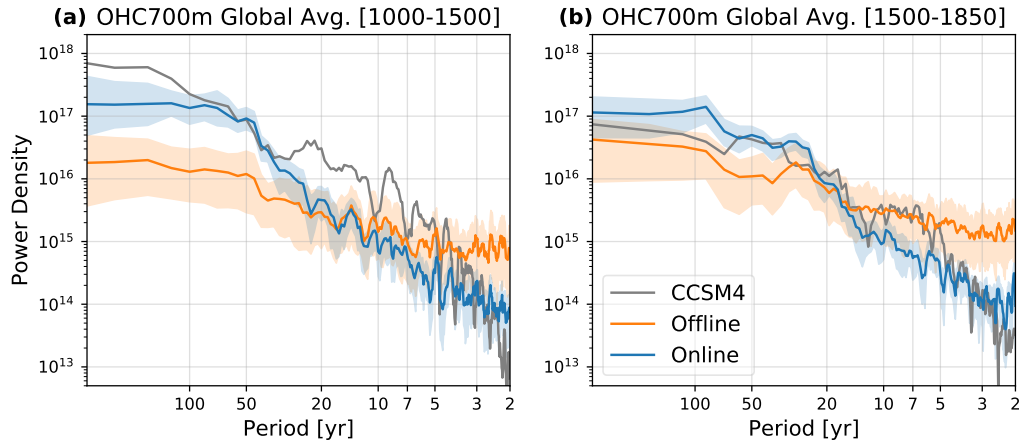


Figure 11. Spectral power density comparison of global average OHC700m between LMR online (CCSM4-LIM) (blue) and offline (orange) reconstructions and reference last millennium simulation data (dark grey) for (a) 1000–1500 C.E. and (b) 1500–1850 C.E. Spectra are calculated from the ensemble mean of each of the 50 reconstruction Monte-Carlo iterations. Solid lines denote the average spectral density while shading shows the 95% confidence interval.

584 The most notable effect from the inclusion of LIM forecasts for online assimilation
 585 is the memory and variability of ocean heat content. Figure 11 shows a spectral power
 586 disparity between the offline and online reconstructions at short and long periods. At
 587 short timescales (periods of 2–3 years), the offline reconstruction shows approximately
 588 an order of magnitude larger variability than the online reconstruction and reference CCSM4
 589 simulation. At longer timescales (periods > 50 years), the offline case has an order of
 590 magnitude less variability than the online reconstruction and CCSM4 reference simu-
 591 lation for OHC700m. This behavior is displayed in both the relatively data-sparse early
 592 period (1000–1500 C.E.) and when more proxy information is available. In the offline
 593 case, the upper-ocean heat content is solely determined by field covariance and the year’s
 594 available proxy observations. The lack of memory means that OHC700m is free to vary
 595 widely between years, but also that it does not necessarily act as a long-term filter of
 596 atmospheric variability (i.e., an ocean layer with a large amount of thermal inertia). The
 597 ensemble average of global mean OHC700m (Fig. 10c) shows the lack of field constraint
 598 in the offline reconstruction. The wide confidence interval relates to a large range of re-
 599 constructed global mean OHC700m in ensemble members, but when averaged across the
 600 ensemble, little coherent low-frequency variability remains. The autocorrelation of the
 601 global average OHC700m (Figs. S9a, S9b) highlights the lack of memory in the offline
 602 reconstruction, where autocorrelations at a two-year lag decrease below 0.4, whereas the
 603 online reconstructions and reference simulations show autocorrelations in the range of
 604 0.8–0.9.

605 We turn now to how the online method affects the relationships between global average
 606 SST and OHC700m (Fig. 12a,b), and the Niño 3.4 and PDO indices (Fig. 12c,d).
 607 The global average SST and OHC lead-lag correlations show online reconstructions have
 608 an asymmetric relationship where SST leads OHC700m. During the data-sparse period
 609 (Fig. 12a), the global average SST correlation with OHC700m at five-years lead is around
 610 0.7, while at five-years lag, the correlations are around 0.4–0.5. The lead-lag relation-
 611 ship from the reference Last Millennium simulations is also asymmetric but with smaller
 612 correlations during this period. SST leading OHC700m implies the atmosphere is driv-
 613 ing the changes in upper-ocean heat content. The offline reconstruction does not display

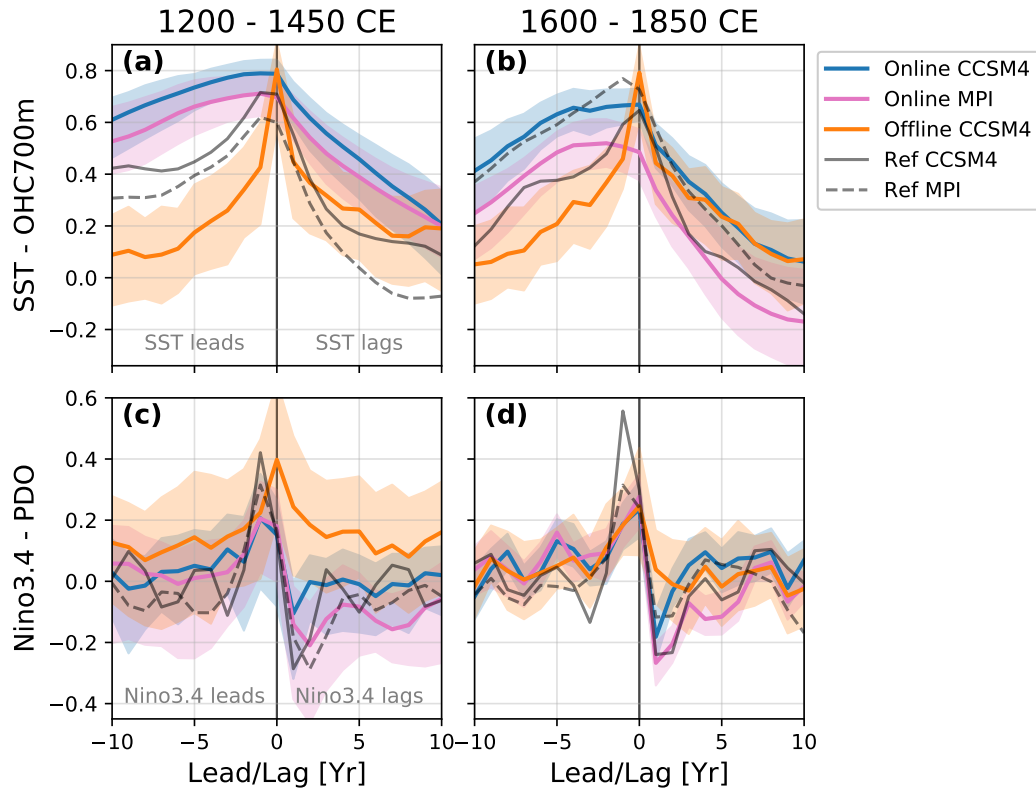


Figure 12. Lead-lag correlations for scalar indices of global average SST and OHC700m (row a) and Niño 3.4 and PDO (row c) for the time periods of 1200–1450 C.E. (column a) and 1600–1850 C.E. (column b). Correlations are shown for the Online CCSM4-LIM (blue) and MPI-LIM (pink) reconstructions, the CCSM4 Offline (orange) reconstruction, and reference last millennium simulation data from the CCSM4 (black solid) and MPI (dashed black) models. Correlations are calculated at the specified lead/lag from the ensemble mean of each of the 50 reconstruction Monte-Carlo iterations. For reconstructions, solid lines denote the average correlation across Monte-Carlo iterations while shading shows the 95% confidence interval.

614 a lead-lag asymmetry and has lower correlation compared to the online reconstructions
615 except at zero-lag.

616 From 1600–1850 C.E., when more proxy information is available, the online recon-
617 struction lead-lag correlations for global mean SST and OHC700m are slightly lower (Fig.
618 12b), with correlations around 0.5–0.6 at an SST-lead of five years, and correlations near
619 0 (MPI-LIM) and 0.3 (CCSM4-LIM) at an SST-lag of 5 years. The online reconstruc-
620 tions still display a correlation asymmetry with higher correlations when SST leads. How-
621 ever, the online SST-lag correlations for the CCSM4-LIM reconstruction closely corre-
622 spond to the SST-lag correlations in the offline case, and the MPI-LIM SST-lag corre-
623 lations are lower than the offline SST-lag correlations. In the offline case, the lead-lag
624 relationship does not qualitatively change between the two periods. The reference sim-
625 ulation lead-lag correlations show differences in magnitude between the periods but re-
626 tain the asymmetric lead-lag character.

627 For the Niño 3.4 and PDO index lead-lag relationships, there is a disparity in the
628 early period between offline and online reconstructions (Fig. 12c) that is rectified, to a
629 degree, with increased proxy record availability (Fig. 12d). During 1200–1450 C.E., the
630 online reconstructions show the Niño 3.4 leads the PDO by one year (correlations near
631 0.2). At a one-year lag, the Niño 3.4 index switches to small anticorrelation. The flip in
632 correlations relates to the timescale difference between ENSO, which oscillates on inter-
633 annual timescales, and the PDO, a more persistent decadal-scale phenomenon. The on-
634 line reconstruction behavior corresponds to a similar lead-lag relationship evident in the
635 reference simulations. The offline reconstruction again shows a symmetric relationship
636 between the indices about zero lag, which is quite different from the online reconstruc-
637 tions.

638 During 1600–1850 C.E., when proxy availability increases, both the offline and on-
639 line reconstructions are quite similar in their Niño 3.4 and PDO lead-lag correlation re-
640 lationships (Fig. 12d), with the largest correlation at zero-lag. A comparison of lead-
641 lag relationships during the instrumental period (\sim 1900–2000 C.E.) also show Niño 3.4
642 and the PDO with the highest correlation occurring at zero-lag, including for the observa-
643 tion-based products (Fig. S10b). The Niño 3.4 phase relationship with the PDO pattern in
644 the North Pacific is suggested to occur via teleconnection responses in the atmospheric
645 circulation (e.g., see review by Newman et al. (2016)). However, recent work isolating
646 variability at different time-frequencies suggests that ENSO and the PDO may be largely
647 independent (Wills et al., 2018). These results suggest the one-year Niño 3.4 lead is a
648 byproduct of the GCM-calibrated LIM and less available proxy data during 1200–1450
649 C.E. When more proxy information is assimilated, the reconstructed PDO–ENSO rela-
650 tionship is in better agreement with observational products. The offline reconstruction
651 does not show the same 1-year-lag anticorrelation as the online results, which suggests
652 that the offline reconstruction constrained only by proxy data may be less likely to switch
653 into La Niña conditions following the positive phase. Overall, these results highlight that
654 when enough data are available to constrain the reconstruction, it is possible that the
655 offline case displays the same temporal dynamics as the online method.

656 7 Discussion of novel reconstruction results

657 Our reconstructions provides novel insight into atmosphere–ocean climate fields over
658 the last millennium based on online data assimilation of paleoclimate proxies. Here we
659 discuss aspects in these results that differ from findings in previous studies. A notable
660 difference compared to previous reconstructions is the finding that the LMR online re-
661 constructions are generally colder by \sim 0.25–0.5 K for NH average TAS and global av-
662 erage SST during the early portion of the last millennium. Additionally, our reconstruc-
663 tions do not show signs of a hemispheric or global-scale warm anomaly during the MCA
664 period, and only a slight millennium-scale cooling trend into the 1800s. The lack of long-

665 term cooling in the LMR online reconstructions contrasts with other temperature recon-
666 structions and climate model simulations over the last millennium (e.g., Figs 8c-f). The
667 small cooling trend with previous statistical reconstruction results should be considered
668 within the context of known sensitivity to methodological choices (e.g., Juckes et al., 2007;
669 Mann et al., 2008), and generally broad uncertainty bounds of previous reconstructions
670 (see Fig. 1a in Neukom, Barboza, et al., 2019). Specifically considering the MCA–LIA
671 differences, the reconstructed pattern of cool tropics and warmer high-latitude regions
672 is in contrast with the primarily global pattern evident in the GCMs. We note that when
673 removing a constant from the the reference GCM results, consistent with the colder global
674 average of the reconstructions, the MCA–LIA difference is more similar. Our sensitiv-
675 ity experiments and the damped-eigenmodes of the LIM forecast (by construction) all
676 point toward the relatively cold reconstructed early temperatures being a result of the
677 dynamical propagation of assimilated proxy information. However, a question for future
678 research concerns whether the reconstructed cool early period is related to the proxy dis-
679 tribution or lack of proxies sensitive to decadal–centennial climate variability.

680 Despite the relatively cold conditions of reconstructed NH average temperature from
681 1000–1250 C.E., the average reconstructed EU temperature displays decadal-scale warm
682 periods, which are approximately half the magnitude of early 20th Century warming.
683 Reconstructed spatial patterns of temperature change between the MCA and LIA pe-
684 riod are spatially heterogeneous, showing large positive anomalies over the Barents Sea
685 and Northern Europe and cooler tropical temperatures. The spatial character of tem-
686 perature differences supports previous results depicting high-latitude warmth and cold
687 tropical temperatures (e.g., Cobb et al., 2003; Mann et al., 2009; Goosse, Crespin, et al.,
688 2012). Examining field regression relationships with average EU temperatures, we find
689 that warm conditions relate to warm SST and OHC700m anomalies over the Norwegian
690 and Barents Seas, and the mid-latitude North Atlantic. Additionally, the atmospheric
691 circulation is characterized by lower SLP across the Arctic and increased mid-latitude
692 ZG500 heights with an upper-level ridge centered over Europe. The reconstruction re-
693 gression relationships notably differ from those derived from the reference simulations
694 (Figs 9c–f) with more broad-scale pan-Arctic circulation connections found in the recon-
695 struction. This again suggests that the assimilated proxies are adding new information
696 about past dynamical relationships compared to unconstrained model simulations. The
697 relation of EU warmth with enhanced lower-level circulations in the reconstruction at
698 least partially supports previous work suggesting longer-term NAO-like circulation anom-
699 alies during the MCA (e.g., Trouet et al., 2009). However, the LMR online reconstruc-
700 tions also suggest major European warm events seem to occur on decadal scales instead
701 of centennial scale during the MCA.

702 Instrumental validation of the reconstructed SST and OHC700m fields show an area
703 of correlations that are consistently low- or anti-correlated in the Labrador Sea and re-
704 gions just south of Greenland and Iceland. This region of weak correlation is also ap-
705 parent in offline reconstructions (Hakim et al., 2016; Tardif et al., 2019). The lack of im-
706 provement with online and offline DA suggests that the climate models used as a basis
707 for field constraints may not correctly represent the variability of this region during the
708 instrumental period, and/or that we do not have enough proxy information to describe
709 this region. In the case of unrepresentative model dynamics, it could mean that instru-
710 mental period covariances related to the North Atlantic are qualitatively different from
711 the pre-industrial period, perhaps related to changes in external forcing. Further inves-
712 tigation into the causes of the reconstruction discrepancy in this region could provide
713 insight into the relative roles of internal ocean dynamics and external forcing in the North
714 Atlantic, which is an active and open research question (e.g., Clement et al., 2015; Zhang
715 et al., 2016; Vecchi et al., 2017; Sutton et al., 2018; Wills et al., 2019).

8 Conclusions

Understanding the dynamics of coupled atmosphere–ocean low frequency variability of the real climate system requires a physically consistent gridded dataset that is faithful, within error, to the climate recorded by proxy archives. We have presented coupled atmosphere–ocean field reconstructions over the last millennium that incorporate temporal constraints from online data assimilation with linear inverse models (LIMs). Global aggregate measures of sea surface temperature (SST) and upper-700m ocean heat content (OHC700m) show relatively cold pre-industrial conditions with pronounced decadal-to-centennial-scale variability. By the modern era, significant increases in temperature and heat content related to anthropogenic greenhouse gas forcing are apparent. As full-field reconstructions, we can calculate and assess a large variety of physically-consistent dynamic field measures and uncertainty over a much longer time period than instrumental data allow. For example, the reconstructed Niño 3.4 index shows millennium-scale warming on the order of ~ 0.5 K per 1000 years. The reconstructed PDO does not display distinct trends or changes to variability from 1600–2000 C.E. Before 1600, there is pronounced decadal-to-centennial-scale variability of the PDO index, potentially related to lower proxy coverage during the early period. We also find regional decadal periods of warm temperatures over northern Europe during the MCA, and from the underlying full-field information, we assess connections to regional circulation via regression against reconstructed atmospheric fields.

Instrumental validation of reconstructed ocean fields shows remarkable agreement given that the results derive from the assimilation of sparsely distributed and mostly terrestrial proxy information. We find high levels of agreement between our reconstruction and instrumental products with global average SST (correlations between 0.8–0.9), upper-700m ocean heat content (OHC700m; correlations greater than 0.9 with two recent products), and Niño 3.4 (correlations near 0.8). The reconstructed PDO shows moderate agreement with instrumental products in the CCSM4-LIM reconstruction (correlations near 0.6), generally capturing the same inter-decadal PDO variability. Furthermore, spatial validation shows broadly positive correlations for the reconstructed SST field and more regionally dependent positive correlations for OHC700m. Encouragingly, we find that our reconstructed surface temperature agrees well with the carefully curated and minimally pre-processed Crowley et al. (2014) reconstruction, and that our reconstruction gives a better estimate of the instrumental surface temperature despite the Crowley reconstruction being calibrated directly to it. Altogether, the positive validation results across many fields and indices give confidence that the reconstruction strategy produces high-fidelity, dynamically-consistent results.

The primary goal of incorporating a forecast model into the LMR framework is to provide further dynamical constraints and allow for dynamical memory of proxy information over time. For global temperature fields, assimilated proxy information suggests colder conditions on average compared to reconstructions constrained only by the proxy record. For reconstructed OHC700m, the memory from the forecast model results in an order of magnitude more power to variability on timescales longer than 50 years and smooths high-frequency fluctuations, compared to the offline case. The enhanced expression of multi-decadal variability, in general, improves one of the primary criticisms of offline reconstruction results, the relatively smooth character of reconstructed global averages. Moreover, the addition of the online forecasts improves aspects of the coupled-field lead-lag relationships in the reconstructions. For global average SST and OHC700m, lead-lag correlations show that SST generally leads OHC700m, which would physically relate to OHC integrating forcing from the ocean surface over time and is in better agreement with the GCMs from which the LIMs are derived. In contrast, the offline reconstruction shows a considerably different relationship with a symmetric peak about zero-lag between global average SST and OHC700m. The Niño 3.4 and PDO lead-lag relationship highlights the addition of dynamical constraints when fewer proxies are avail-

769 able. In the earlier period from 1200–1450 C.E., the online reconstructions show sim-
 770 ilar characteristics as in the GCM simulations with Niño 3.4 leading the PDO by one
 771 year, whereas the offline reconstruction again shows symmetric lead–lag correlations. Dur-
 772 ing later periods, when more proxy records are available, the offline reconstruction changes
 773 character with a lead–lag relationship between Niño 3.4 and PDO similar to online re-
 774 constructions, highlighting the dependence on observations without the forecast model.

775 This extension of the LMR framework to include online data assimilation repre-
 776 sents a significant step forward in combining information from proxies with climate model
 777 constraints. The approach promotes easy comparison of various GCM dynamics, pro-
 778 vides an easy pathway to update reconstructions as new model simulations become avail-
 779 able, and accommodates new information from expanded proxy databases (e.g., Ander-
 780 son et al., 2019). For example, using two different GCM-calibrated (CCSM4 and MPI)
 781 we compare and contrast reconstructed state of past climate as a check of result robust-
 782 ness. While we focused on validation and description of specific ocean fields, the recon-
 783 structions include other fields, which can also be used for investigations of coupled vari-
 784 ability over the last millennium, validation against observations and climate models, and
 785 comparisons with previous reconstructions. For example, we have used the results here
 786 to show that the time period of the MCA was in fact much colder than previously es-
 787 timated in the hemispheric-mean temperature and that it was a regional phenomenon
 788 over Northern Europe. Moreover, the circulation pattern we find in the reconstruction
 789 departs significantly from that in last-millennium climate model simulations, which un-
 790 derscores the importance of proxy records in estimating the actual climate behavior. Sim-
 791 ilarly, when compared to last-millennium climate model simulations, the reconstructions
 792 show a greater influence of SST leading changes in OHC, and a weaker relationship be-
 793 tween the Niño 3.4 and PDO indices (Fig. 11). These findings illustrate the power of this
 794 approach: by combining proxies and online DA, we discover dynamical insights into the
 795 climate system that differ from those in the climate model. Since climate models have
 796 different expressions of coupled atmosphere–ocean variability (e.g., Branstator et al., 2012),
 797 including the proxy records is essential.

798 In this work, we focus on DA-based reconstructions over the Common Era, which
 799 features relatively broad proxy coverage and many coincident GCM simulations. For deeper
 800 time DA application (e.g., Tierney et al., 2020), significant non-stationarity related to
 801 external forcing complicates the GCM modeling such that further research is needed to
 802 determine how to best formulate and apply a statistical forecast method like a LIM. For
 803 the Common Era, there are a further improvements we envision, including the assim-
 804 ilation of multi-resolution records (e.g., Steiger & Hakim, 2016) in PDA, such as the Ocean2k
 805 sediment records (McGregor et al., 2015), which would likely provide better centennial
 806 and millennial-scale constraints than from annual timescale proxies alone. Furthermore,
 807 other fields with slow-timescales of variability, such as sea ice, might be similarly improved
 808 using an online assimilation method for field reconstruction.

809 Appendix A EnKF Vector Solver

810 Here we present the vector solver for the ensemble Kalman update equation, which
 811 is a variant of the ensemble transform Kalman filter described by Bishop et al. (2002).
 812 When using ensembles to estimate sample statistics (e.g., prior covariance, \mathbf{B}), the Kalman
 813 update equation (Eq. 1) describes an update of the ensemble average. The state, \mathbf{x} , is
 814 an $M \times 1$ row vector equal to the the column average of, \mathbf{X} , the $M \times N$ state ensem-
 815 ble. Here, M represents the number of state features (e.g., field grid points) and N is
 816 the number of ensemble members. Equivalently, the estimated observations, \mathbf{y}_e (with di-
 817 mensions $P \times 1$ where P is the number of proxies) represent the column average of the
 818 ensemble of proxy estimates calculated on $\mathcal{H}(\mathbf{X})$. For paleoclimate reconstruction, it is
 819 usually the case that the number of state features is much larger than the number of ob-
 820 servations ($M \gg P$), which suggests that the updated state will be at least partially

821 under-determined. The vector transform reduces the problem into the smaller space ($O(N \times$
 822 $P)$) by diagonalizing \mathbf{K} and creating linear combinations of proxy observations.

823 To translate the problem into a transformed space, we define $\tilde{\mathbf{x}} = \mathbf{B}^{-1/2}\mathbf{x}$ and $\tilde{\mathbf{y}} =$
 824 $\mathbf{R}^{-1/2}\mathbf{y}$ and substitute into Eq. 1, giving

$$\tilde{\mathbf{x}}_a = \tilde{\mathbf{x}}_b + \tilde{\mathbf{K}}[\tilde{\mathbf{y}} - \tilde{\mathbf{H}}\tilde{\mathbf{x}}_b] \quad (\text{A1})$$

825 where

$$\begin{aligned} \mathbf{B}^{1/2} &= \frac{1}{\sqrt{N-1}} [\mathbf{X} - \bar{\mathbf{X}}], \\ \tilde{\mathbf{H}} &= \mathbf{R}^{-1/2}\mathbf{H}\mathbf{B}^{1/2}, \\ \tilde{\mathbf{K}} &= \tilde{\mathbf{H}}^T [\tilde{\mathbf{H}}\tilde{\mathbf{H}}^T + \mathbf{I}]^{-1}. \end{aligned}$$

826 We then perform a singular value decomposition on $\tilde{\mathbf{H}}$ ($\tilde{\mathbf{H}} = \mathbf{U}\mathbf{\Lambda}\mathbf{V}^T$) and transform
 827 into the new component space using

$$\begin{aligned} \hat{\mathbf{x}} &= \mathbf{V}^T\tilde{\mathbf{x}} \\ \hat{\mathbf{y}} &= \mathbf{U}^T\tilde{\mathbf{y}}. \end{aligned}$$

828 Converting equation A1 into the new coordinates yields

$$\hat{\mathbf{x}}_a = \hat{\mathbf{x}}_b + \hat{\mathbf{K}}[\hat{\mathbf{y}} - \mathbf{\Lambda}\hat{\mathbf{x}}_b], \quad (\text{A2})$$

829 where

$$\hat{\mathbf{K}} = \mathbf{\Lambda} [\mathbf{\Lambda}^2 + \mathbf{I}]^{-1}, \quad (\text{A3})$$

830 In this optimal space, the update considers all proxies and properly weights information
 831 between ensemble members in a single calculation. The weighting term, $\mathbf{\Lambda}$ ($P \times N$), is
 832 a diagonal matrix with terms in order of influence. The optimal space state ($\hat{\mathbf{x}}$) has di-
 833 mensions of $N \times 1$ and observations ($\hat{\mathbf{y}}$) has dimensions $P \times 1$. To translate from the
 834 optimal space state back to the full space for results, we calculate

$$\mathbf{X}_a = \mathbf{X}_b\mathbf{V}\hat{\mathbf{x}}_a. \quad (\text{A4})$$

835 Appendix B Linear Inverse Models

836 For the benefit of the reader, we summarize a technical background description of
 837 LIMs, their calibration, and stochastic integration in Appendix B1, and in Appendix B2,
 838 we summarize the multivariate LIM calibration strategy described in Perkins and Hakim
 839 (2020).

840 B1 Background

841 A linear inverse model (LIM, Penland & Sardeshmukh, 1995) is an empirically de-
 842 termined estimate of a dynamical system linearized about its mean state. In this model,

$$\frac{d\mathbf{x}}{dt} = \mathbf{L}\mathbf{x} + \boldsymbol{\xi}, \quad (\text{B1})$$

843 the slow-varying deterministic drift of the state is explicitly defined by the matrix oper-
 844 ator, \mathbf{L} , while fast-timescale processes are represented as white-noise forcing, $\boldsymbol{\xi}$. We
 845 use this simple model to create a coupled GCM analog to forecast multivariate states
 846 between reconstructed times.

847 To create a LIM, we perform an empirical fit based on 1-year lag-covariance ($\tau =$
 848 1) statistics of the climate state,

$$\mathbf{L} = \tau^{-1} \ln[\mathbf{C}(\tau)\mathbf{C}(0)^{-1}], \quad (\text{B2})$$

849 with the sample n -lag covariance defined as $\mathbf{C}(n) = \langle \mathbf{x}(n)\mathbf{x}^T(0) \rangle$. Note that angle brack-
 850 ets represent an expectation, which in practice is taken as a sample average. The dynam-
 851 ical operator, \mathbf{L} , encapsulates the information to propagate predictable aspects of the
 852 state from one time to the next. System dynamics are assumed to be stable, which re-
 853 quires that the forecast modes (i.e., eigenvectors of \mathbf{L}) of a valid LIM do not grow with
 854 time. While constructive interference between forecast modes enables short-term tran-
 855 sient anomaly growth (e.g., ENSO), extended deterministic forecasts asymptote to zero
 856 if all modes are damped. For applications in EnKF assimilation, the forecast ensemble
 857 variance is crucial for weighting the prior against and the innovation from observations.
 858 LIM deterministic forecasts alone (omitting the noise term, $\boldsymbol{\xi}$) have collapsing forecast
 859 ensemble variance over time, which limits the utilization of observations.

860 In Perkins and Hakim (2017), forecast ensemble variance is enhanced by blending
 861 the LIM ensemble forecast with climatological covariances from a GCM, using a “hybrid”
 862 DA method adapted from Hamill and Snyder (2000). This technique incorporates a blend-
 863 ing coefficient, which is tuned based on reconstruction results, to control the amount of
 864 information from the forecast and climatological source. More recently, PH20 use a LIM
 865 as a GCM analog for coupled ocean–atmosphere ensemble forecasts and find that stochas-
 866 tic LIM forecasts reasonably approximate the ensemble variance and errors at 1-year lead
 867 times. Stochastic integration provides a natural mechanism to sample the envelope of
 868 noise-forced spread across assimilation times, and it does not necessarily require a tun-
 869 ing procedure based on reconstruction output. Moreover, integration provides a straight-
 870 forward technique for providing time-variable information that is potentially useful for
 871 more sophisticated PSMs in the future. For these reasons, we choose to utilize a LIM
 872 with stochastic noise forcing ($\boldsymbol{\xi}$) to sustain ensemble variance between assimilation times.

873 To perform stochastic LIM forecasts, we first determine the noise forcing statistics
 874 of the system, $\mathbf{Q} = \langle \boldsymbol{\xi}\boldsymbol{\xi}^T \rangle dt$, using the calibration data. With the assumption of sta-
 875 tionary statistics, we use the dynamical operator, \mathbf{L} (Eq. B2), and the fluctuation–dissipation
 876 relationship (Penland & Matrosova, 1994),

$$\frac{d\mathbf{C}(0)}{dt} = \mathbf{L}\mathbf{C}(0) + \mathbf{C}(0)\mathbf{L}^T + \mathbf{Q} = 0, \quad (\text{B3})$$

877 to estimate \mathbf{Q} . With both model terms (\mathbf{L} and \mathbf{Q}) we explicitly simulate the determin-
 878 istic and stochastic drift of a sample climate trajectory over time using a two-step in-
 879 tegration scheme defined by Penland and Matrosova (1994),

$$\mathbf{a}(t + \delta t) = \mathbf{L}\mathbf{x}(t) + \hat{\mathbf{Q}}\sqrt{\Lambda\delta t}\boldsymbol{\alpha} \quad (\text{B4})$$

$$\mathbf{x}(t + \delta t/2) = [\mathbf{x}(t) + \mathbf{a}(t + \delta t)]/2. \quad (\text{B5})$$

880 In this scheme, \mathbf{a} is an intermediate state variable, $\hat{\mathbf{Q}}$ and $\mathbf{\Lambda}$ are from the eigendecom-
 881 position $\mathbf{Q} = \hat{\mathbf{Q}}\mathbf{\Lambda}\hat{\mathbf{Q}}^{-1}$, δt is the timestep, and $\boldsymbol{\alpha}$ is a vector of random numbers drawn
 882 from a unit-normal distribution.

883 B2 Parameter Reduction and Calibration

884 Climate-scale predictability is typically dominated by a few modes of atmosphere-
 885 ocean variability such as ENSO, the PDO, and Atlantic multidecadal variability. There-
 886 fore, the number of important degrees of freedom for the predictable climate state are
 887 substantially fewer than the total degrees of freedom presented by the gridded climate
 888 fields of the climate model. For this reason, we consolidate the information of the grid-
 889 ded climate fields for use in LIM forecasting by using a two-step EOF reduction as in
 890 PH20, which we summarize here.

891 The climate state, \mathbf{X} , used for reconstruction includes target output fields and also
 892 fields required for estimated observation calculations via PSMs. These fields are concate-
 893 nated along the first dimension to form the total state,

$$\mathbf{X} = \begin{bmatrix} \mathbf{X}_1 \\ \mathbf{X}_2 \\ \vdots \\ \mathbf{X}_F \end{bmatrix}.$$

894 For the initial step, we reduce each of the F fields individually. We first area weight each
 895 row of field \mathbf{X}_f (with dimensions of spatial features by ensemble samples, $m \times n$), in this
 896 case using latitude weighting,

$$\mathbf{x}_i^w = \mathbf{x}_i \sqrt{\cos(\phi_i)} \quad \text{for } i = 1, \dots, m,$$

897 where ϕ_i represents the i^{th} grid cell latitude. We then find the EOFs truncated to the
 898 leading k modes, \mathbf{U}_f , using a singular value decomposition (SVD), $\mathbf{X}_f^w = \mathbf{U}_f \boldsymbol{\Sigma}_f \mathbf{V}_f^T$,
 899 and project the field into this space using: $\hat{\mathbf{X}}_f = \mathbf{U}_f^T \mathbf{X}_f^w$. The initial reduction com-
 900 pactly represents fields and expedites the next step's multivariate-EOF calculation.

901 For the second reduction, we first standardize each field by the total component
 902 variance, σ_f , and reform the state using previously reduced fields,

$$\hat{\mathbf{X}} = \begin{bmatrix} \hat{\mathbf{X}}_1/\sigma_1 \\ \hat{\mathbf{X}}_2/\sigma_2 \\ \vdots \\ \hat{\mathbf{X}}_F/\sigma_F \end{bmatrix}.$$

903 Then we take the SVD of this new state, $\hat{\mathbf{X}} = \hat{\mathbf{U}}\hat{\boldsymbol{\Sigma}}\hat{\mathbf{V}}^T$, and use the leading ℓ EOFs to
 904 project into the components of the fully reduced multivariate-EOF state, $\tilde{\mathbf{X}} = \hat{\mathbf{U}}^T \hat{\mathbf{X}}$.
 905 The LIM calibration procedure (Eq. B2) and forecasts (Eqs. B4,B5) take place using
 906 data projected into the reduced space defined by $\tilde{\mathbf{X}}$. By storing the EOFs and standard-
 907 ization factors ($\hat{\mathbf{U}}$, \mathbf{U}_f , and σ_f), we project into and out of the space during the recon-
 908 struction process.

909 The reduction process introduces two parameters, k and ℓ , determining the EOF
 910 truncation at each step. For our experiments, we choose to retain the leading 400 EOFs
 911 ($k = 400$) in the first step, which we find retains greater than 90% of each field's vari-
 912 ance. The second reduction parameter ultimately determines the LIM skill properties

913 and ensemble forecast spread characteristics (Perkins & Hakim, 2020). As in PH20, we
 914 separate OHC700m from the multivariate reduction process due to adverse effects on fore-
 915 cast skill from truncation. The leading OHC700m field components from the first reduc-
 916 tion (retaining 20 modes) are instead appended to the multivariate state to form the LIM-
 917 space components,

$$\mathbf{z} = \begin{bmatrix} \tilde{\mathbf{X}} \\ \hat{\mathbf{X}}_{OHC} \end{bmatrix}.$$

918 We additionally find that due to the small magnitude of values in the PR field, which
 919 have similar scale as numerical errors of the EOF-reduction procedure, it is useful to stan-
 920 dardize precipitation values by the total field variance before the first step reduction.

921 With additional fields in the state vector compared to PH20, including all season-
 922 ally averaged TAS fields, we run the same diagnostic tests for increasing numbers of re-
 923 tained multivariate-EOF components investigating both aggregate measures of 1-year
 924 forecast skill and ensemble calibration. We get similar results as in PH20 that the fore-
 925 cast skill of aggregate measures (e.g., global averages, ENSO, and the PDO) are posi-
 926 tive and do not substantially change after retaining 15–20 multivariate-EOF components
 927 (not shown). Ensemble characteristics are prone to unpredictable changes at different
 928 multivariate-EOF truncations due to an imperfectly determined \mathbf{L} (e.g., from noise and
 929 non-linearity), which similarly affects the determination of \mathbf{Q} and leads to numerical un-
 930 certainty in the eigendecomposition of the noise statistics (PH20). Therefore, we per-
 931 form tests to assess the ensemble calibration ratios (see supplementary text Section S1)
 932 for global averages (TAS, SST, OHC700m) and dynamic indices (PDO- and ENSO-related
 933 quantities). The calibration ratio gives a measure indicating whether the ensemble vari-
 934 ance is representative of the forecast errors where a “well-calibrated” ensemble forecast
 935 system would result in a ratio near 1.0. Based on calibration ratio results, we select the
 936 multivariate-EOF truncation parameter of $\ell = 20$ for the CCSM4-LIM, and $\ell = 27$
 937 for the MPI-LIM.

938 Appendix C PSM Objective Seasonality Determination

939 For proxy PSMs, we use univariate linear regression models, $y_{ek} = \beta_{0k} + \beta_{1k}\bar{x} +$
 940 ϵ_k , fit to temperature data estimate proxy values for the k^{th} proxy, y_{ek} (e.g., tree-ring
 941 widths), from the climate state, \bar{x} . The overbar (e.g., \bar{x}) denotes a seasonal-to-annual
 942 average of the temperature using data from the closest grid cell from calibration data.
 943 We determine the time-average distinction used for each PSM by a series of objective
 944 seasonality tests for tree-based proxies (as in Tardif et al., 2019), and use the PAGES2017
 945 seasonality metadata for all other proxies. We fit parameters including the intercept (β_{0k}),
 946 slope (β_{1k}) and Gaussian error with statistics $\mathcal{N}(0, \sigma_k^2)$ through a least-squares fit with
 947 co-located temperature data in the NASA Goddard Institute for Space Studies Surface
 948 Temperature Analysis GISTEMP v4 (Hansen et al., 2010) dataset (similarly regridded
 949 to a $2^\circ \times 2^\circ$ grid). Note that the proxy error variances (σ_k^2), which are assumed to be
 950 independent, form the diagonal of the proxy error covariance matrix, \mathbf{R} . The objective
 951 determination of seasonality for tree-based proxies involves a series of tests across pre-
 952 scribed seasonal averages (Jan–Dec, JJA, JJASON, DJF, DJFMAM, AMJJAS, OND-
 953 JFM) and the expert-derived seasonality in the PAGES2017 database. We then make
 954 a selection of the seasonal-average definition with the best overall calibration fit from the
 955 tests. The best fit is defined as the model with the lowest-value Bayesian information
 956 criterion, $BIC = -2\ln(\hat{L}) + k\ln(n)$ (Schwarz, 1978), where \hat{L} is the maximum value
 957 from the likelihood function of the model, k is the model’s number of estimated param-
 958 eters, and n is the sample size.

959 **Acronyms**

960	CCSM4 Community Climate System Model version 4
961	CCSM4-LIM CCSM4-calibrated LIM
962	CFR climate field reconstruction
963	DA data assimilation
964	EG13 Emile-Geay et al. (2013a)
965	EnKF ensemble Kalman filter
966	EOF empirical orthogonal function
967	GCM global climate model
968	LIA Little Ice Age
969	LIM linear inverse model
970	LMR Last Millennium Reanalysis
971	MCA Medieval Climate Anomaly
972	MPI Max Planck Institute Earth System Model
973	MPI-LIM MPI-calibrated LIM
974	OHC700m 0–700 m ocean heat content
975	PAGES2017 PAGES 2k Consortium (2017)
976	PDA paleoclimate data assimilation
977	PDO Pacific Decadal Oscillation
978	PH20 Perkins and Hakim (2020)
979	PR precipitation
980	PSM proxy system model
981	RLUT outgoing TOA longwave radiation
982	RSUT outgoing TOA shortwave radiation
983	SLP sea-level pressure
984	SSS sea-surface salinity
985	SST sea-surface temperature
986	TAS 2 m surface air temperature
987	TOA top of atmosphere
988	ZG500 500 hPa geopotential heights
989	ZOS dynamic ocean surface height

990 **Acknowledgments**

991 The authors thank Robert Tardif for his contributions to the LMR codebase, many of
992 which are adapted for this online version. Chris Snyder (NCAR) originated the idea for
993 the vector solver described in Appendix A. The comparison of our results to Crowley
994 et al. (2014) was suggested by an anonymous reviewer and the Associate Editor. We thank
995 three anonymous reviewers, the Associate Editor, and the Editor for their feedback on
996 the manuscript. This research was supported by Heising-Simons Foundation grant 2016-
997 014, and National Science Foundation (NSF) grants AGS-1602223, AGS-1702423 made
998 by the to the University of Washington. The first author was supported by the National
999 Science Foundation Graduate Research Fellowship under grant no. DGE-1256082.

1000 The CMIP5 climate model data was obtained through the Lawrence Livermore Na-
1001 tional Laboratory Earth System Grid Federation Portal
1002 (<https://esgf-node.llnl.gov/projects/esgf-llnl/>). The reconstruction framework used to
1003 perform the experiments can be found online at <https://github.com/frodre/LMROnline>
1004 (<https://doi.org/10.5281/zenodo.4563364>). The linear inverse modeling code can be found
1005 at

1006 <https://github.com/frodre/pyLIM> (<http://doi.org/10.5281/zenodo.3243749>). Selected
 1007 reconstruction data, analysis code, and pre-processed LMR input data are available at
 1008 <http://doi.org/10.5281/zenodo.4563663>.

1009 References

- 1010 Alexander, M. A., Matrosova, L., Penland, C., Scott, J. D., & Chang, P. (2008, jan).
 1011 Forecasting Pacific SSTs: Linear Inverse Model Predictions of the PDO. *Jour-*
 1012 *nal of Climate*, *21*(2), 385–402. doi: 10.1175/2007JCLI1849.1
- 1013 Ambaum, M. H. P., Hoskins, B. J., & Stephenson, D. B. (2001, aug). Arctic Os-
 1014 cillation or North Atlantic Oscillation? *Journal of Climate*, *14*(16), 3495–3507.
 1015 doi: 10.1175/1520-0442(2001)014(3495:AOONAO)2.0.CO;2
- 1016 Ammann, C. M., Joos, F., Schimel, D. S., Otto-Bliesner, B. L., & Tomas, R. A.
 1017 (2007). Solar influence on climate during the past millennium: Results
 1018 from transient simulations with the NCAR Climate System Model. *Pro-*
 1019 *ceedings of the National Academy of Sciences*, *104*(10), 3713–3718. doi:
 1020 10.1073/pnas.0605064103
- 1021 Anderson, D. M., Tardif, R., Horlick, K., Erb, M. P., Hakim, G. J., Noone, D., ...
 1022 Steig, E. (2019). Additions to the Last Millennium Reanalysis Multi-Proxy
 1023 Database. *Data Science Journal*, *18*(1), 2. doi: 10.5334/dsj-2019-002
- 1024 Atwood, A. R., Wu, E., Frierson, D. M. W., Battisti, D. S., & Sachs, J. P. (2016,
 1025 feb). Quantifying Climate Forcings and Feedbacks over the Last Millennium
 1026 in the CMIP5–PMIP3 Models*. *Journal of Climate*, *29*(3), 1161–1178. doi:
 1027 10.1175/JCLI-D-15-0063.1
- 1028 Balmaseda, M. A., Mogensen, K., & Weaver, A. T. (2013). Evaluation of the
 1029 ECMWF ocean reanalysis system ORAS4. *Quarterly Journal of the Royal*
 1030 *Meteorological Society*, *139*(674), 1132–1161. doi: 10.1002/qj.2063
- 1031 Bhend, J., Franke, J., Folini, D., Wild, M., & Brönnimann, S. (2012, may). An
 1032 ensemble-based approach to climate reconstructions. *Climate of the Past*, *8*(3),
 1033 963–976. doi: 10.5194/cp-8-963-2012
- 1034 Biondi, F., Gershunov, A., & Cayan, D. R. (2001). North Pacific Decadal Climate
 1035 Variability since 1661. *Journal of Climate*, *14*(1), 5–10. doi: 10.1175/1520-
 1036 -0442(2001)014(0005:NPDCVS)2.0.CO;2
- 1037 Bishop, C. H., Etherton, B. J., & Majumdar, S. J. (2002). Adaptive Sampling with
 1038 the Ensemble Transform Kalman Filter. Part I: Theoretical Aspects. *Monthly*
 1039 *Weather Review*, *129*(3), 420–436. doi: 10.1175/1520-0493(2001)129(0420:
 1040 aswtet)2.0.co;2
- 1041 Branstator, G., Teng, H., Meehl, G. A., Kimoto, M., Knight, J. R., Latif, M.,
 1042 & Rosati, A. (2012). Systematic estimates of initial-value decadal pre-
 1043 dictability for six AOGCMs. *Journal of Climate*, *25*(6), 1827–1846. doi:
 1044 10.1175/JCLI-D-11-00227.1
- 1045 Broecker, W. S. (2001, feb). PALEOCLIMATE: Was the Medieval Warm Period
 1046 Global? *Science*, *291*(5508), 1497–1499. doi: 10.1126/science.291.5508.1497
- 1047 Chang, Y. S., Zhang, S., Rosati, A., Delworth, T. L., & Stern, W. F. (2013).
 1048 An assessment of oceanic variability for 1960–2010 from the GFDL ensem-
 1049 ble coupled data assimilation. *Climate Dynamics*, *40*(3–4), 775–803. doi:
 1050 10.1007/s00382-012-1412-2
- 1051 Cheng, L., Trenberth, K. E., Fasullo, J., Boyer, T., Abraham, J., & Zhu, J. (2017).
 1052 Improved estimates of ocean heat content from 1960 to 2015. *Science Ad-*
 1053 *vances*, *3*(3), 1–11. doi: 10.1126/sciadv.1601545
- 1054 Clement, A., Bellomo, K., Murphy, L. N., Cane, M. A., Mauritsen, T., Radel,
 1055 G., & Stevens, B. (2015, oct). The Atlantic Multidecadal Oscillation
 1056 without a role for ocean circulation. *Science*, *350*(6258), 320–324. doi:
 1057 10.1126/science.aab3980
- 1058 Cobb, K. M., Charles, C. D., Cheng, H., & Edwards, R. L. (2003, jul). El

- 1059 Niño/Southern Oscillation and tropical Pacific climate during the last mil-
 1060 lennium. *Nature*, 424(6946), 271–276. doi: 10.1038/nature01779
- 1061 Compo, G. P., Whitaker, J. S., Sardeshmukh, P. D., Matsui, N., Allan, R. J., Yin,
 1062 X., . . . Worley, S. J. (2011, jan). The Twentieth Century Reanalysis Project.
 1063 *Quarterly Journal of the Royal Meteorological Society*, 137(654), 1–28. doi:
 1064 10.1002/qj.776
- 1065 Crespin, E., Goosse, H., Fichet, T., & Mann, M. E. (2009). The 15th century Arctic
 1066 warming in coupled model simulations with data assimilation. *Climate of
 1067 the Past*, 5(3), 389–401. doi: 10.5194/cp-5-389-2009
- 1068 Crowley, T. J., Obrochta, S. P., & Liu, J. (2014, may). Recent global temperature
 1069 “plateau” in the context of a new proxy reconstruction. *Earth’s Future*, 2(5),
 1070 281–294. doi: 10.1002/2013EF000216
- 1071 D’Arrigo, R., Villalba, R., & Wiles, G. (2001). Tree-ring estimates of Pacific
 1072 decadal climate variability. *Climate Dynamics*, 18(3-4), 219–224. doi:
 1073 10.1007/s003820100177
- 1074 D’Arrigo, R., & Wilson, R. (2006). On the Asian expression of the PDO. *Interna-
 1075 tional Journal of Climatology*, 26(12), 1607–1617. doi: 10.1002/joc.1326
- 1076 de Boissésou, E., Balmaseda, M. A., & Mayer, M. (2018). Ocean heat content vari-
 1077 ability in an ensemble of twentieth century ocean reanalyses. *Climate Dynam-
 1078 ics*, 50(9-10), 3783–3798. doi: 10.1007/s00382-017-3845-0
- 1079 Diaz, H. F., Trigo, R., Hughes, M. K., Mann, M. E., Xoplaki, E., & Barriopedro,
 1080 D. (2011, nov). Spatial and Temporal Characteristics of Climate in Medieval
 1081 Times Revisited. *Bulletin of the American Meteorological Society*, 92(11),
 1082 1487–1500. doi: 10.1175/BAMS-D-10-05003.1
- 1083 Dubinkina, S., Goosse, H., Sallaz-Damaz, Y., Crespin, E., & Crucifix, M. (2011,
 1084 dec). Testing a Particle Filter to Reconstruct Climate Changes Over the Past
 1085 Centuries. *International Journal of Bifurcation and Chaos*, 21(12), 3611–3618.
 1086 doi: 10.1142/S0218127411030763
- 1087 Duchon, C. E. (1979, aug). Lanczos Filtering in One and Two Dimensions. *Jour-
 1088 nal of Applied Meteorology*, 18(8), 1016–1022. doi: 10.1175/1520-0450(1979)
 1089 018<1016:LFIOAT>2.0.CO;2
- 1090 Emile-Geay, J., Cobb, K. M., Mann, M. E., & Wittenberg, A. T. (2013a, apr).
 1091 Estimating Central Equatorial Pacific SST Variability over the Past Millen-
 1092 nium. Part II: Reconstructions and Implications. *Journal of Climate*, 26(7),
 1093 2329–2352. doi: 10.1175/JCLI-D-11-00511.1
- 1094 Emile-Geay, J., Cobb, K. M., Mann, M. E., & Wittenberg, A. T. (2013b, apr). Es-
 1095 timating Central Equatorial Pacific SST Variability over the Past Millennium.
 1096 Part I: Methodology and Validation. *Journal of Climate*, 26(7), 2302–2328.
 1097 doi: 10.1175/JCLI-D-11-00510.1
- 1098 Esper, J., Cook, E. R., & Schweingruber, F. H. (2002). Low-frequency signals in
 1099 long tree-ring chronologies for reconstructing past temperature variability. *Sci-
 1100 ence*, 295(5563), 2250–2253. doi: 10.1126/science.1066208
- 1101 Evensen, G. (2003). The Ensemble Kalman Filter: Theoretical formulation and
 1102 practical implementation. *Ocean Dynamics*, 53(4), 343–367. doi: 10.1007/
 1103 s10236-003-0036-9
- 1104 Franke, J., Brönnimann, S., Bhend, J., & Brugnara, Y. (2017). A monthly global
 1105 paleo-reanalysis of the atmosphere from 1600 to 2005 for studying past cli-
 1106 matic variations. *Scientific Data*, 4, 1–19. doi: 10.1038/sdata.2017.76
- 1107 Giorgetta, M. A., Jungclaus, J., Reick, C. H., Legutke, S., Bader, J., Böttinger,
 1108 M., . . . Stevens, B. (2013). Climate and carbon cycle changes from 1850 to
 1109 2100 in MPI-ESM simulations for the Coupled Model Intercomparison Project
 1110 phase 5. *Journal of Advances in Modeling Earth Systems*, 5(3), 572–597. doi:
 1111 10.1002/jame.20038
- 1112 Good, S. A., Martin, M. J., & Rayner, N. A. (2013). EN4: Quality controlled
 1113 ocean temperature and salinity profiles and monthly objective analyses with

- 1114 uncertainty estimates. *Journal of Geophysical Research: Oceans*, 118(12),
 1115 6704–6716. doi: 10.1002/2013JC009067
- 1116 Goosse, H. (2017). Reconstructed and simulated temperature asymmetry between
 1117 continents in both hemispheres over the last centuries. *Climate Dynamics*,
 1118 48(5-6), 1483–1501. doi: 10.1007/s00382-016-3154-z
- 1119 Goosse, H., Crespin, E., de Montety, a., Mann, M. E., Renssen, H., & Timmermann,
 1120 a. (2010). Reconstructing surface temperature changes over the past 600 years
 1121 using climate model simulations with data assimilation. *Journal of Geophysical
 1122 Research*, 115, 1–17. doi: 10.1029/2009JD012737
- 1123 Goosse, H., Crespin, E., Dubinkina, S., Loutre, M. F., Mann, M. E., Renssen, H., ...
 1124 Shindell, D. (2012). The role of forcing and internal dynamics in explaining
 1125 the "Medieval Climate Anomaly". *Climate Dynamics*, 39(12), 2847–2866. doi:
 1126 10.1007/s00382-012-1297-0
- 1127 Goosse, H., Guiot, J., Mann, M. E., Dubinkina, S., & Sallaz-Damaz, Y. (2012).
 1128 The medieval climate anomaly in Europe: Comparison of the summer
 1129 and annual mean signals in two reconstructions and in simulations with
 1130 data assimilation. *Global and Planetary Change*, 84-85, 35–47. doi:
 1131 10.1016/j.gloplacha.2011.07.002
- 1132 Hakim, G. J., Emile-Geay, J., Steig, E. J., Noone, D., Anderson, D. M., Tardif, R.,
 1133 ... Perkins, W. A. (2016). The Last Millennium Climate Reanalysis Project:
 1134 Framework and First Results. *Journal of Geophysical Research: Atmospheres*.
 1135 doi: 10.1002/2016JD024751
- 1136 Hamill, T. M., & Snyder, C. (2000). A Hybrid Ensemble Kalman Filter–3D Varia-
 1137 tional Analysis Scheme. *Monthly Weather Review*, 128(8), 2905–2919. doi: 10
 1138 .1175/1520-0493(2000)128<2905:AHEKFV>2.0.CO;2
- 1139 Hansen, J., Ruedy, R., Sato, M., & Lo, K. (2010). Global surface temperature
 1140 change. *Rev. Geophys.*, 48(4), RG4004. doi: 10.1029/2010RG000345.1
 1141 .INTRODUCTION
- 1142 Hasselmann, K. (1976). Stochastic climate models Part I. Theory. *Tellus*, 28(6),
 1143 473–485. doi: 10.3402/tellusa.v28i6.11316
- 1144 Hawkins, E., & Sutton, R. (2009). Decadal predictability of the Atlantic
 1145 Ocean in a coupled GCM: Forecast skill and optimal perturbations us-
 1146 ing linear inverse modeling. *Journal of Climate*, 22(14), 3960–3978. doi:
 1147 10.1175/2009JCLI2720.1
- 1148 Huntley, H. S., & Hakim, G. J. (2010, nov). Assimilation of time-averaged observa-
 1149 tions in a quasi-geostrophic atmospheric jet model. *Climate Dynamics*, 35(6),
 1150 995–1009. doi: 10.1007/s00382-009-0714-5
- 1151 Jukes, M. N., Allen, M. R., Briffa, K. R., Esper, J., Hegerl, G. C., Moberg, A.,
 1152 ... Weber, S. L. (2007, oct). Millennial temperature reconstruction in-
 1153 tercomparison and evaluation. *Climate of the Past*, 3(4), 591–609. doi:
 1154 10.5194/cp-3-591-2007
- 1155 Laloyaux, P., de Boisseson, E., Balmaseda, M., Bidlot, J. R., Broennimann, S.,
 1156 Buizza, R., ... Schepers, D. (2018). CERA-20C: A Coupled Reanalysis of the
 1157 Twentieth Century. *Journal of Advances in Modeling Earth Systems*, 10(5),
 1158 1172–1195. doi: 10.1029/2018MS001273
- 1159 Lamb, H. H. (1965). The early medieval warm epoch and its sequel. *Palaeogeogra-
 1160 phy, Palaeoclimatology, Palaeoecology*, 1, 13–37.
- 1161 Landrum, L., Otto-Bliesner, B. L., Wahl, E. R., Conley, A., Lawrence, P. J.,
 1162 Rosenbloom, N., & Teng, H. (2013). Last Millennium Climate and
 1163 Its Variability in CCSM4. *Journal of Climate*, 26(4), 1085–1111. doi:
 1164 10.1175/JCLI-D-11-00326.1
- 1165 Ljungqvist, F. C. (2010, sep). A new reconstruction of temperature variability in the
 1166 extra-tropical northern hemisphere during the last two millennia. *Geografiska
 1167 Annaler: Series A, Physical Geography*, 92(3), 339–351. doi: 10.1111/j.1468
 1168 -0459.2010.00399.x

- 1169 MacDonald, G. M., & Case, R. A. (2005). Variations in the Pacific Decadal Oscilla-
1170 tion over the past millennium. *Geophysical Research Letters*, *32*(8), 1–4. doi:
1171 10.1029/2005GL022478
- 1172 Mann, M. E., Bradley, R. S., & Hughes, M. K. (1999). *Northern hemisphere tem-*
1173 *peratures during the past millennium: Inferences, uncertainties, and limitations*
1174 (Vol. 26). doi: 10.1029/1999GL900070
- 1175 Mann, M. E., & Jones, P. D. (2003). Global surface temperatures over the past
1176 two millennia. *Geophysical Research Letters*, *30*(15), 15–18. doi: 10.1029/
1177 2003GL017814
- 1178 Mann, M. E., Zhang, Z., Hughes, M. K., Bradley, R. S., Miller, S. K., Ruther-
1179 ford, S., & Ni, F. (2008). Proxy-based reconstructions of hemispheric and
1180 global surface temperature variations over the past two millennia. *Pro-*
1181 *ceedings of the National Academy of Sciences*, *105*(36), 13252–13257. doi:
1182 10.1073/pnas.0805721105
- 1183 Mann, M. E., Zhang, Z., Rutherford, S., Bradley, R. S., Hughes, M. K., Shindell, D.,
1184 ... Ni, F. (2009, nov). Global Signatures and Dynamical Origins of the Little
1185 Ice Age and Medieval Climate Anomaly. *Science*, *326*(5957), 1256–1260. doi:
1186 10.1126/science.1177303
- 1187 Mantua, N. J., Hare, S. R., Zhang, Y., Wallace, J. M., & Francis, R. C. (1997).
1188 A Pacific Interdecadal Climate Oscillation with Impacts on Salmon Produc-
1189 tion. *Bulletin of the American Meteorological Society*, *78*(6), 1069–1079. doi:
1190 10.1175/1520-0477(1997)078<1069:APICOW>2.0.CO;2
- 1191 Matsikaris, A., Widmann, M., & Jungclaus, J. (2015, jan). On-line and off-line data
1192 assimilation in palaeoclimatology: a case study. *Climate of the Past*, *11*(1),
1193 81–93. doi: 10.5194/cp-11-81-2015
- 1194 Matsikaris, A., Widmann, M., & Jungclaus, J. (2016a, jun). Assimilating continental
1195 mean temperatures to reconstruct the climate of the late pre-industrial period.
1196 *Climate Dynamics*, *46*(11-12), 3547–3566. doi: 10.1007/s00382-015-2785-9
- 1197 Matsikaris, A., Widmann, M., & Jungclaus, J. (2016b). Influence of proxy data un-
1198 certainty on data assimilation for the past climate. *Climate of the Past*, *12*(7),
1199 1555–1563. doi: 10.5194/cp-12-1555-2016
- 1200 McGregor, H. V., Evans, M. N., Goosse, H., Leduc, G., Martrat, B., Addison, J. A.,
1201 ... Ersek, V. (2015). Robust global ocean cooling trend for the pre-industrial
1202 Common Era. *Nature Geoscience*, *8*(9), 671–677. doi: 10.1038/ngeo2510
- 1203 Meehl, G. A., Arblaster, J. M., Matthes, K., Sassi, F., & Van Loon, H. (2009).
1204 Amplifying the pacific climate system response to a small 11-year solar cycle
1205 forcing. *Science*, *325*(5944), 1114–1118. doi: 10.1126/science.1172872
- 1206 Moberg, A., Sonechkin, D. M., Holmgren, K., Datsenko, M. H., & Karlén, W.
1207 (2005). Highly variable Northern Hemisphere temperatures reconstructed
1208 from low- and high-resolution proxy data. *Nature*, *433*(7026), 613–617. doi:
1209 10.1038/nature03265
- 1210 Neukom, R., Barboza, L. A., Erb, M. P., Shi, F., Emile-Geay, J., Evans, M. N., ...
1211 Von Gunten, L. (2019, aug). Consistent multidecadal variability in global
1212 temperature reconstructions and simulations over the Common Era. *Na-*
1213 *ture Geoscience*, *12*(8), 643–649. Retrieved from [http://www.nature.com/
1214 articles/s41561-019-0400-0](http://www.nature.com/articles/s41561-019-0400-0) doi: 10.1038/s41561-019-0400-0
- 1215 Neukom, R., Steiger, N., Gómez-Navarro, J. J., Wang, J., & Werner, J. P. (2019,
1216 jul). No evidence for globally coherent warm and cold periods over the
1217 preindustrial Common Era. *Nature*, *571*(7766), 550–554. doi: 10.1038/
1218 s41586-019-1401-2
- 1219 Newman, M. (2013, jul). An Empirical Benchmark for Decadal Forecasts of Global
1220 Surface Temperature Anomalies. *Journal of Climate*, *26*(14), 5260–5269. doi:
1221 10.1175/JCLI-D-12-00590.1
- 1222 Newman, M., Alexander, M. A., Ault, T. R., Cobb, K. M., Deser, C., Di Lorenzo,
1223 E., ... Smith, C. A. (2016). The Pacific decadal oscillation, revisited. *Journal*

- 1224 *of Climate*, 29(12), 4399–4427. doi: 10.1175/JCLI-D-15-0508.1
- 1225 Newman, M., Alexander, M. A., & Scott, J. D. (2011). An empirical model of trop-
1226 ical ocean dynamics. *Climate Dynamics*, 37(9-10), 1823–1841. doi: 10.1007/
1227 s00382-011-1034-0
- 1228 Okazaki, A., & Yoshimura, K. (2017). Development and evaluation of a system of
1229 proxy data assimilation for paleoclimate reconstruction. *Climate of the Past*,
1230 13(4), 379–393. doi: 10.5194/cp-13-379-2017
- 1231 Oke, P. R. (2002). Assimilation of surface velocity data into a primitive equation
1232 coastal ocean model. *Journal of Geophysical Research*, 107(C9), 3122. doi: 10
1233 .1029/2000JC000511
- 1234 Oke, P. R., Sakov, P., & Corney, S. P. (2007, jan). Impacts of localisation in the
1235 EnKF and EnOI: experiments with a small model. *Ocean Dynamics*, 57(1),
1236 32–45. doi: 10.1007/s10236-006-0088-8
- 1237 Oke, P. R., Schiller, A., Griffin, D. A., & Brassington, G. B. (2005, oct). Ensemble
1238 data assimilation for an eddy-resolving ocean model of the Australian region.
1239 *Quarterly Journal of the Royal Meteorological Society*, 131(613), 3301–3311.
1240 doi: 10.1256/qj.05.95
- 1241 Osborn, T. J., Jones, P. D., Lister, D. H., Morice, C. P., Simpson, I. R., Winn, J. P.,
1242 ... Harris, I. C. (2021, jan). Land Surface Air Temperature Variations Across
1243 the Globe Updated to 2019: The CRUTEM5 Data Set. *Journal of Geophysical*
1244 *Research: Atmospheres*, 126(2). doi: 10.1029/2019JD032352
- 1245 PAGES 2k Consortium. (2017). A global multiproxy database for temperature re-
1246 constructions of the Common Era. *Scientific Data*, 4(170088), 1–33. doi: DOI:
1247 10.1038/sdata.2017.88
- 1248 Pendergrass, A. G., Hakim, G. J., Battisti, D. S., & Roe, G. (2012, jan). Cou-
1249 pled Air–Mixed Layer Temperature Predictability for Climate Reconstruction.
1250 *Journal of Climate*, 25(2), 459–472. doi: 10.1175/2011JCLI4094.1
- 1251 Penland, C., & Matrosova, L. (1994). *A Balance Condition for Stochastic Numerical*
1252 *Models with Application to the El Niño–Southern Oscillation* (Vol. 7) (No. 9).
1253 doi: 10.1175/1520-0442(1994)007(1352:ABCFSN)2.0.CO;2
- 1254 Penland, C., & Sardeshmukh, P. D. (1995, aug). The Optimal Growth of Tropical
1255 Sea Surface Temperature Anomalies. *Journal of Climate*, 8(8), 1999–2024. doi:
1256 10.1175/1520-0442(1995)008(1999:TOGOTS)2.0.CO;2
- 1257 Perkins, W. A., & Hakim, G. (2020). Linear inverse modeling for coupled
1258 atmosphere–ocean ensemble climate prediction. *Journal of Advances*
1259 *in Modeling Earth Systems*, 12(1), e2019MS001778. (e2019MS001778
1260 10.1029/2019MS001778) doi: 10.1029/2019MS001778
- 1261 Perkins, W. A., & Hakim, G. J. (2017). Reconstructing paleoclimate fields using on-
1262 line data assimilation with a linear inverse model. *Climate of the Past*, 13(5),
1263 421–436. doi: 10.5194/cp-13-421-2017
- 1264 Poli, P., Hersbach, H., Dee, D. P., Berrisford, P., Simmons, A. J., Vitart, F., ...
1265 Fisher, M. (2016). ERA-20C: An atmospheric reanalysis of the twentieth cen-
1266 tury. *Journal of Climate*, 29(11), 4083–4097. doi: 10.1175/JCLI-D-15-0556.1
- 1267 Pollack, H. N., & Smerdon, J. E. (2004). Borehole climate reconstructions: Spatial
1268 structure and hemispheric averages. *Journal of Geophysical Research D: Atmo-*
1269 *spheres*, 109(11), 1–9. doi: 10.1029/2003JD004163
- 1270 Riser, S. C., Freeland, H. J., Roemmich, D., Wijffels, S., Troisi, A., Belbéoch, M., ...
1271 Jayne, S. R. (2016). Fifteen years of ocean observations with the global Argo
1272 array. *Nature Climate Change*, 6(2), 145–153. doi: 10.1038/nclimate2872
- 1273 Rogers, J. C. (1997). North Atlantic storm track variability and its association
1274 to the North Atlantic oscillation and climate variability of Northern Europe.
1275 *Journal of Climate*, 10(7), 1635–1647. doi: 10.1175/1520-0442(1997)010(1635:
1276 NASTVA)2.0.CO;2
- 1277 Rutherford, S., Mann, M. E., Osborn, T. J., Briffa, K. R., Jones, P. D., Bradley,
1278 R. S., & Hughes, M. K. (2005, jul). Proxy-Based Northern Hemisphere Surface

- 1279 Temperature Reconstructions: Sensitivity to Method, Predictor Network, Tar-
 1280 get Season, and Target Domain. *Journal of Climate*, 18(13), 2308–2329. doi:
 1281 10.1175/JCLI3351.1
- 1282 Schwarz, G. (1978). Estimating the Dimension of a Model. *The Annals of Statistics*,
 1283 6(2), 461–464.
- 1284 Shen, C., Wang, W. C., Gong, W., & Hao, Z. (2006). A Pacific Decadal Os-
 1285 cillation record since 1470 AD reconstructed from proxy data of summer
 1286 rainfall over eastern China. *Geophysical Research Letters*, 33(3), 1–4. doi:
 1287 10.1029/2005GL024804
- 1288 Singh, H. K. A., Hakim, G. J., Tardif, R., Emile-Geay, J., & Noone, D. C. (2017).
 1289 Atlantic Multidecadal Variability from the Last Millennium Reanalysis. *Cli-
 1290 mate of the Past Discussions*, 1–25. doi: 10.5194/cp-2017-49
- 1291 Steiger, N. J., & Hakim, G. (2016, jun). Multi-timescale data assimilation for atmo-
 1292 sphere–ocean state estimates. *Climate of the Past*, 12(6), 1375–1388. doi: 10
 1293 .5194/cp-12-1375-2016
- 1294 Steiger, N. J., Hakim, G. J., Steig, E. J., Battisti, D. S., & Roe, G. H. (2014). As-
 1295 similation of Time-Averaged Pseudoproxies for Climate Reconstruction. *Jour-
 1296 nal of Climate*, 27, 426–441. doi: 10.1175/JCLI-D-12-00693.1
- 1297 Steiger, N. J., Smerdon, J. E., Cook, E. R., & Cook, B. I. (2018). A reconstruction
 1298 of global hydroclimate and dynamical variables over the Common Era. *Scien-
 1299 tific Data*, 5, 1–15. doi: 10.1038/sdata.2018.86
- 1300 Sutton, R. T., McCarthy, G. D., Robson, J., Sinha, B., Archibald, A. T., & Gray,
 1301 L. J. (2018, feb). Atlantic Multidecadal Variability and the U.K. ACSIS Pro-
 1302 gram. *Bulletin of the American Meteorological Society*, 99(2), 415–425. doi:
 1303 10.1175/BAMS-D-16-0266.1
- 1304 Tardif, R., Hakim, G. J., Perkins, W. A., Horlick, K. A., Erb, M. P., Emile-Geay, J.,
 1305 ... Noone, D. (2019, jul). Last Millennium Reanalysis with an expanded proxy
 1306 database and seasonal proxy modeling. *Climate of the Past*, 15(4), 1251–1273.
 1307 doi: 10.5194/cp-15-1251-2019
- 1308 Tardif, R., Hakim, G. J., & Snyder, C. (2014). Coupled atmosphere-ocean data
 1309 assimilation experiments with a low-order climate model. *Climate Dynamics*,
 1310 43(5-6), 1631–1643. doi: 10.1007/s00382-013-1989-0
- 1311 Taylor, K. E., Stouffer, R. J., & Meehl, G. a. (2012). An overview of CMIP5 and
 1312 the experiment design. *Bulletin of the American Meteorological Society*, 93(4),
 1313 485–498. doi: 10.1175/BAMS-D-11-00094.1
- 1314 Tierney, J. E., Zhu, J., King, J., Malevich, S. B., Hakim, G. J., & Poulsen, C. J.
 1315 (2020, aug). Glacial cooling and climate sensitivity revisited. *Nature*,
 1316 584(7822), 569–573. doi: 10.1038/s41586-020-2617-x
- 1317 Trigo, R. M., Osborn, T. J., & Corte-Real, J. M. (2002). The North Atlantic
 1318 Oscillation influence on Europe: Climate impacts and associated physical
 1319 mechanisms. *Climate Research*, 20(1), 9–17. doi: 10.3354/cr020009
- 1320 Trouet, V., Esper, J., Graham, N. E., Baker, A., Scourse, J. D., & Frank, D. C.
 1321 (2009, apr). Persistent Positive North Atlantic Oscillation Mode Dom-
 1322 inated the Medieval Climate Anomaly. *Science*, 324(5923), 78–80. doi:
 1323 10.1126/science.1166349
- 1324 Vecchi, G. A., Delworth, T. L., & Booth, B. (2017, aug). Origins of Atlantic decadal
 1325 swings. *Nature*, 548(7667), 284–285. doi: 10.1038/nature23538
- 1326 Wallace, J. M., & Thompson, D. W. J. (1998). The Arctic oscillation signature
 1327 in the wintertime geopotential height and temperature fields. *Geophysical Re-
 1328 search Letters*, 25(9), 1297–1300.
- 1329 Wang, J., Emile-Geay, J., Guillot, D., McKay, N. P., & Rajaratnam, B. (2015).
 1330 Fragility of reconstructed temperature patterns over the Common Era: Impli-
 1331 cations for model evaluation. *Geophysical Research Letters*, 42(17), 7162–7170.
 1332 doi: 10.1002/2015GL065265
- 1333 Whitaker, J., & Hamill, T. (2002). Ensemble data assimilation without perturbed

- 1334 observations. *Monthly Weather Review*, 1913–1924.
- 1335 Wills, R. C., Armour, K. C., Battisti, D. S., & Hartmann, D. L. (2019). Ocean-
1336 atmosphere dynamical coupling fundamental to the atlantic multidecadal oscil-
1337 lation. *Journal of Climate*, 32(1), 251–272. doi: 10.1175/JCLI-D-18-0269.1
- 1338 Wills, R. C., Schneider, T., Wallace, J. M., Battisti, D. S., & Hartmann, D. L.
1339 (2018). Disentangling Global Warming, Multidecadal Variability, and El Niño
1340 in Pacific Temperatures. *Geophysical Research Letters*, 45(5), 2487–2496. doi:
1341 10.1002/2017GL076327
- 1342 Zanna, L. (2012). Forecast skill and predictability of observed atlantic sea surface
1343 temperatures. *Journal of Climate*, 25(14), 5047–5056. doi: 10.1175/JCLI-D-11
1344 -00539.1
- 1345 Zanna, L., Khatiwala, S., Gregory, J. M., Ison, J., & Heimbach, P. (2019, jan).
1346 Global reconstruction of historical ocean heat storage and transport. *Pro-
1347 ceedings of the National Academy of Sciences*, 116(4), 1126–1131. doi:
1348 10.1073/pnas.1808838115
- 1349 Zhang, R., Sutton, R., Danabasoglu, G., Delworth, T. L., Kim, W. M., Robson, J.,
1350 & Yeager, S. G. (2016, jun). Comment on "The Atlantic Multidecadal Oscilla-
1351 tion without a role for ocean circulation". *Science*, 352(6293), 1527–1527. doi:
1352 10.1126/science.aaf1660